



Magnetic Fields in the Early Stages of Massive Star Formation as Revealed by ALMA

Junhao Liu^{1,2,3}, Qizhou Zhang³, Keping Qiu^{1,2}, Haiyu Baobab Liu⁴, Thushara Pillai^{5,6}, Josep Miquel Girart^{7,8}, Zhi-Yun Li⁹, and Ke Wang¹⁰

¹ School of Astronomy and Space Science, Nanjing University, 163 Xianlin Avenue, Nanjing 210023, People's Republic of China; kpqiu@nju.edu.cn

² Key Laboratory of Modern Astronomy and Astrophysics (Nanjing University), Ministry of Education, Nanjing 210023, People's Republic of China

³ Center for Astrophysics | Harvard & Smithsonian, 60 Garden Street, Cambridge, MA 02138, USA

⁴ Academia Sinica Institute of Astronomy and Astrophysics, P.O. Box 23-141, Taipei 10617, Taiwan

⁵ Max-Planck-Institut für Radioastronomie, Auf dem Hügel 69, D-53121 Bonn, Germany

⁶ Institute for Astrophysical Research, 725 Commonwealth Ave, Boston University Boston, MA 02215, USA

⁷ Institut de Ciències de l'Espai (ICE, CSIC), Can Magrans s/n, E-08193 Cerdanyola del Vallès, Catalonia, Spain

⁸ Institut d'Estudis Espacials de Catalunya (IEEC), E-08034 Barcelona, Catalonia, Spain

⁹ Astronomy Department, University of Virginia, Charlottesville, VA 22904-4325, USA

¹⁰ Kavli Institute for Astronomy and Astrophysics, Peking University, 5 Yiheyuan Road, Haidian District, Beijing 100871, People's Republic of China

Received 2020 February 3; revised 2020 April 25; accepted 2020 May 4; published 2020 June 5

Abstract

We present 1.3 mm ALMA dust polarization observations at a resolution of ~ 0.02 pc for three massive molecular clumps, MM1, MM4, and MM9, in the infrared dark cloud G28.34+0.06. With these sensitive and high-resolution continuum data, MM1 is resolved into a cluster of condensations. The magnetic field structure in each clump is revealed by the polarized emission. We found a trend of decreasing polarized emission fraction with increasing Stokes I intensities in MM1 and MM4. Using the angular dispersion function method (a modified Davis–Chandrasekhar–Fermi method), the plane-of-sky magnetic field strengths in two massive dense cores, MM1-Core1 and MM4-Core4, are estimated to be ~ 1.6 mG and ~ 0.32 mG, respectively. The virial parameters in MM1-Core1 and MM4-Core4 are calculated to be ~ 0.76 and ~ 0.37 , respectively, suggesting that massive star formation does not start in equilibrium. Using the polarization-intensity gradient-local gravity method, we found that the local gravity is closely aligned with intensity gradient in the three clumps, and the magnetic field tends to be aligned with the local gravity in MM1 and MM4 except for regions near the emission peak, which suggests that the gravity plays a dominant role in regulating the gas collapse. Half of the outflows in MM4 and MM9 are found to be aligned within 10° of the condensation-scale (< 0.05 pc) magnetic field, indicating that the magnetic field could play an important role from condensation to disk scale in the early stage of massive star formation.

Unified Astronomy Thesaurus concepts: [Polarimetry \(1278\)](#); [Magnetic fields \(994\)](#); [Star formation \(1569\)](#); [Infrared dark clouds \(787\)](#)

1. Introduction

It is clear that stars are formed from the collapse of molecular dense cores¹¹ that are created by the contraction of overdense regions in molecular clouds when gravity overcomes internal pressures such as magnetic fields or turbulence (Shu et al. 1987). In the formation of massive stars (mass $> 8 M_\odot$), turbulence is believed to play an important role because massive star-forming regions are usually found to be supersonic and have large line widths. However, the role of magnetic fields in massive star formation is still not well understood (Krumholz 2014; Tan et al. 2014; Hull & Zhang 2019; Pattle & Fissel 2019).

The Radiative Alignment Torque (RAT) theory predicts that asymmetrical dust grains with sizes $> 0.05 \mu\text{m}$ are expected to spin-up due to the radiative torque in the presence of a radiation field and the short axis of these dust grains would tend to be aligned with magnetic field lines (Lazarian 2007; Lazarian & Hoang 2007). Theoretical and observational evidence has supported the RAT mechanism as the dominant grain alignment mechanism to produce polarized thermal emission at millimeter/submillimeter (mm/submm) wavelengths in diffuse interstellar medium and

molecular clouds with μm or sub- μm size grains (Andersson et al. 2015). The exception is that the grain size grows to millimeter/submillimeter in protoplanetary disks and the observed polarization would be dominated by those produced from dust self-scattering (Kataoka et al. 2015; Yang et al. 2016) or grains aligned by strong radiation fields (Tazaki et al. 2017). Thus, observing the polarized dust emission at mm/submm wavelengths offers a powerful way to trace the plane-of-sky magnetic field in star-forming molecular clouds at scales greater than the disk scales.

In the past two decades, there has been an increasing number of high-resolution and high-sensitivity observational studies of the dust polarization in high-mass star-forming regions (for a detailed review, see Hull & Zhang 2019). A variety of field structures from hourglass-like shapes, e.g., G31.41, G240.31, and OMC 1 (Girart et al. 2009; Qiu et al. 2014; Ward-Thompson et al. 2017), to more complex and chaotic morphologies, e.g., Orion KL and G5.89 (Rao et al. 1998; Tang et al. 2009), have been reported by these studies. The magnetic field in massive star-forming regions is found to be dynamically important from the clump scale to the core scale and the core scale magnetic field does not show strong correlation with the outflow axis (Zhang et al. 2014). Quantitatively, the magnetic field plays an important role in supporting the massive dense cores against gravitational collapse (Girart et al. 2013; Frau et al. 2014).

¹¹ Following the nomenclature in Zhang et al. (2009), we define a molecular clump as an entity of ~ 1 pc, a dense core as an entity of ~ 0.1 pc, and a condensation as an entity of ~ 0.01 pc that forms one star or a group of stars.

Despite the significant progress made by the recent polarization observations of massive star formation regions, most of these studies of magnetic fields targeted evolved star-forming regions. Due to the relatively weak polarized dust emission and the limitation of instrumental sensitivity, there are only a handful of single-dish case studies about the magnetic field in early massive star formation regions (Pillai et al. 2015; Juvela et al. 2018; Liu et al. 2018b; Soam et al. 2019; Tang et al. 2019) and there is only one interferometric study of the magnetic field at the onset of massive star formation in the infrared dark cloud (IRDC) 18310-4 where the magnetic field structure is not well resolved (Beuther et al. 2018). The role of magnetic fields in the initial stage of massive star formation remains an open question.

There are two distinct models of massive star formation. The turbulent core accretion model (McKee & Tan 2002) envisioned that massive stars are formed via the monolithic collapse of massive dense cores in virial equilibrium, where the pressure support comes from turbulence and the magnetic field (Tan et al. 2013). Alternatively, the competitive accretion model (Bonnell et al. 1997) proposed that a cluster of low-mass protostars compete with one another to accrete from the natal gas reservoir, and the protostars near the center of gravitational potential accreting at higher rates can thus form massive stars. Krumholz et al. (2005) showed that a subvirial state is required for the competitive accretion. Thus, the dynamical state of massive dense cores needs to be measured in order to distinguish between the two models.

IRDCs, which were first identified as dark regions against the diffuse mid-infrared emission in the Galactic plane (Perault et al. 1996), are believed to harbor the early phase of massive star formation. Recent observations and stability analyses of IRDCs show that the turbulence and the thermal pressure are too weak to provide enough support against the gravity in dense clumps and dense cores (Pillai et al. 2011; Zhang et al. 2015; Ohashi et al. 2016; Sanhueza et al. 2017; Lu et al. 2018), suggesting that magnetic fields must provide significant support to bring the core to equilibrium—or that massive star formation are not in equilibrium. Thus, observational studies of the magnetic field in IRDCs are critical to address the question: does massive star formation start in equilibrium?

At a kinematic distance of ~ 4.8 kpc, G28.34+0.06 (hereafter G28.34) is a massive ($>10^4 M_\odot$) filamentary IRDC that harbors more than ten massive (10^2 – $10^3 M_\odot$) molecular clumps (Carey et al. 1998; Pillai et al. 2006; Rathborne et al. 2006; Simon et al. 2006; Butler & Tan 2009; Lin et al. 2017; Wang 2018). Three prominent clumps, MM1 (also referred to as P2, C9, or Dragon-Head), MM4 (also referred to as P1, C2, or Dragon-Belly), and MM9 (also referred to as S, C1, or Dragon-Tail) are revealed from millimeter dust continuum and midinfrared extinction maps (Rathborne et al. 2006; Butler & Tan 2009). All the three clumps are associated with water masers (Wang et al. 2006, 2008) and outflows (Wang et al. 2011; Zhang et al. 2015; Feng et al. 2016a, and this work), indicating that star formation has already begun. The large gas reservoir makes them potential sites to study clustered massive star formation.

The three massive clumps are found to be in different evolutionary stages. With low temperatures (~ 15 K; Wang 2018), high CO depletion (Feng et al. 2016b), and high level of deuteration (Chen et al. 2010), the $70 \mu\text{m}$ dark clump MM9 appears to be in an early stage of massive star formation.

MM9 is resolved into two dense cores: C1-N and C1-S, also referred to as S-B and S-A (Tan et al. 2013; Feng et al. 2016b), where the south core, C1-S, further fragments into two protostellar condensations, C1-Sa and C1-Sb (Tan et al. 2016). MM4 has a temperature of ~ 16 K (Wang et al. 2008) and is associated with an IR-bright protostellar source with a luminosity of $152 L_\odot$ (Ragan et al. 2012). With high-resolution dust continuum observations, the MM4 clump is resolved into six dense cores (MM4-Core1 through MM4-Core6) along the main filament and each core further fragments into several condensations (Zhang et al. 2009; Wang et al. 2011; Zhang et al. 2015; Kong 2019). The more energetic outflow activities, CH_3OH maser detections, less deuterium fraction, and higher luminosity in MM4 indicate that MM4 is more evolved than MM9 (Feng et al. 2019). The MM1 clump is warmer (~ 30 K; Wang et al. 2008) than MM4 and MM9 and is associated with an IR-bright protostellar source with a luminosity of $2950 L_\odot$ (Ragan et al. 2012). Previous dust continuum observations have resolved MM1 into two fragments, P2-SMA1 and P2-SMA2 (Zhang et al. 2009). The rich organic molecular line emissions in P2-SMA1 indicate that it might be a hot molecular core (Zhang et al. 2009). These observations suggest that MM1 is at a later stage of massive star formation than MM4.

We present 1.3 mm Atacama Large Millimeter/submillimeter Array (ALMA) polarization observations toward clumps MM1, MM4, and MM9 in this paper. In Section 2, we summarize the observation and data reduction. In Section 3, we present maps of dust continuum, polarized dust emission, and molecular line emission, and derive the magnetic field strength. In Section 4, we discuss the dynamical state, outflow-magnetic field alignment, and fragmentation, and we compare the orientations of magnetic fields, local gravity (LG), and intensity gradient (IG). In Section 5, we provide a summary of this paper.

2. Observation

Figure 1 presents an overview of G28.34 in the IRAM-30 m 1.3 mm dust continuum (Rathborne et al. 2006). The observations of three massive clumps (MM1, MM4, MM9) in G28.34 were carried out with the ALMA between 2017 April 18 and 2018 June 29 under projects 2016.1.00248.S (Cycle 4; PI: Zhang) and 2017.1.00793.S (Cycle 5; PI: Zhang). An ALMA execution on 2017 April 21 under project 2016.1.00248.S was failed due to some correlator issues and was not used for our analysis. Tables 1 and 2 list the detailed information of the observations. The total on-source time is 17 minutes for MM1 and 17 minutes (in C40-3 or C43-3 configuration) + 8 minutes (in C43-1 configuration) for each fields of MM4 and MM9. The receiver was tuned to cover frequencies ~ 215.5 – 219.5 GHz and ~ 232.5 – 234.5 GHz (band 6), with a total bandwidth of 5.6 GHz (three basebands, with 1.875 GHz effective bandwidth each) for the dust continuum emission in the full polarization mode. Four spectral windows in another baseband were set to cover the CO (2-1), OCS (19-18), ^{13}CS (5-4), and N_2D^+ (3-2) lines with a channel width of 122 kHz (0.16 km s^{-1}) over a bandwidth of 58.6 MHz ($\sim 76 \text{ km s}^{-1}$).

The data taken in 2017 April 18 were manually calibrated by the authors using the Common Astronomy Software Applications (CASA; McMullin et al. 2007), and the rest of the data were calibrated by the ALMA supporting staff. The systematic flux uncertainty of ALMA at Band 6 due to calibration is $\sim 10\%$. We performed two iterations of phase-only self-calibrations on the continuum data using the CASA. The

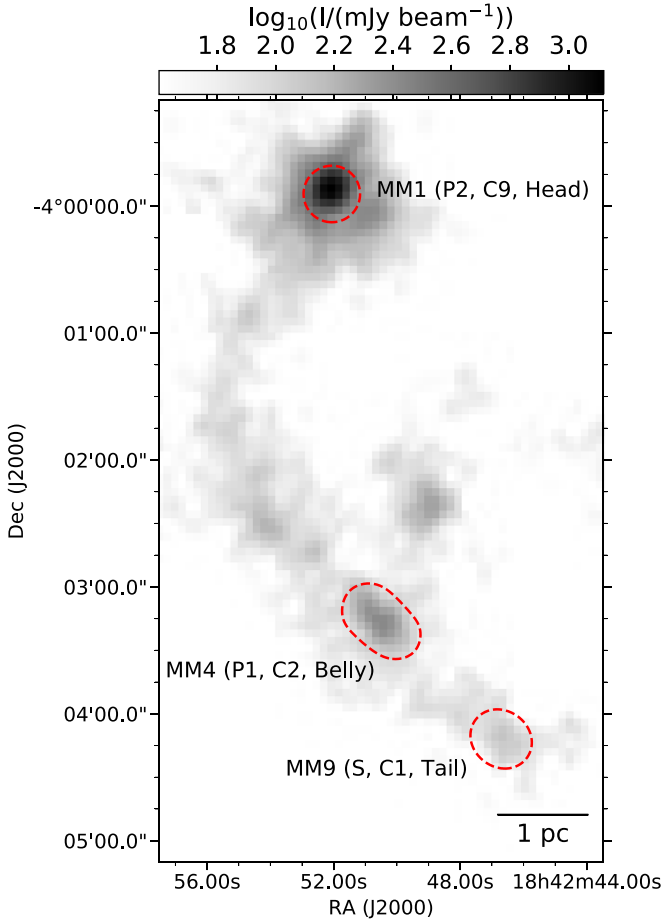


Figure 1. Overview of the IRDC G28.34 (the Dragon Nebula). Gray scale shows the IRAM-30 m 1.2 mm dust continuum of G28.34 with a resolution of $11''$ (Rathborne et al. 2006). Red dashed contours indicate the Full Width at Half-Maximum (FWHM) field of view of our ALMA observations.

Table 1
Source Coordinates

Source	Field	α_{J2000}	δ_{J2000}
MM1	MM1	$18^{\text{h}} 42^{\text{m}} 52^{\text{s}} .06$	$-03^{\circ} 59' 54''.7$
MM4	MM4_1	$18^{\text{h}} 42^{\text{m}} 51^{\text{s}} .05$	$-04^{\circ} 03' 08''.6$
	MM4_2	$18^{\text{h}} 42^{\text{m}} 50^{\text{s}} .69$	$-04^{\circ} 03' 13''.4$
	MM4_3	$18^{\text{h}} 42^{\text{m}} 50^{\text{s}} .39$	$-04^{\circ} 03' 19''.0$
	MM4_4	$18^{\text{h}} 42^{\text{m}} 49^{\text{s}} .88$	$-04^{\circ} 03' 24''.5$
MM9	MM9_1	$18^{\text{h}} 42^{\text{m}} 46^{\text{s}} .48$	$-04^{\circ} 04' 14''.3$
	MM9_2	$18^{\text{h}} 42^{\text{m}} 46^{\text{s}} .91$	$-04^{\circ} 04' 09''.3$

molecular line cubes and Stokes I , Q , and U maps of dust continuum were produced from the visibility data using the CASA task *TCLEAN* with a Briggs weighting parameter of $\text{robust} = 0.5$. The maps for MM4 and MM9 are constructed from a four-pointing mosaic of MM4_1, MM4_2, MM4_3, and MM4_4, and a two-pointing mosaic of MM9_1 and MM9_2, respectively. The synthesized beams of the maps are $0''.8\text{--}0''.9 \times 0''.6\text{--}0''.7$ ($\sim 0.02\text{--}0.015$ pc at a source distance of 4.8 kpc). The maximum recoverable scale¹² is $\sim 7''$ (~ 0.14 pc

at 4.8 kpc) for MM1 and $\sim 13''$ (~ 0.3 pc at 4.8 kpc) for MM4 and MM9. After primary beam correction, the 1σ rms noises of the Stokes I maps of dust continuum reach ~ 300 , 80, and $60 \mu\text{Jy}/\text{beam}$ for MM1, MM4, and MM9, respectively, while the the Stokes Q/U maps have rms noises of $\sim 35 \mu\text{Jy}/\text{beam}$ for MM1 and $\sim 15 \mu\text{Jy}/\text{beam}$ for MM4 and MM9. The sensitivities of the primary beam response-corrected spectral line cubes for MM1, MM4, and MM9 are ~ 2.2 , 1.2, and $1.4 \text{ mJy}/\text{beam}$, respectively, with a velocity channel width of 0.5 km s^{-1} .

Because the polarized intensity and polarized percentage are defined as positive values, the measured quantities of the two parameters are biased toward larger values (Vaillancourt 2006). The debiased polarized intensity PI and its corresponding uncertainty σ_{PI} are calculated as:

$$\text{PI} = \sqrt{Q^2 + U^2 - \sigma_{Q/U}^2}, \quad (1)$$

and

$$\sigma_{\text{PI}} = \sqrt{2} \sigma_{Q/U}, \quad (2)$$

where $\sigma_{Q/U}$ is the 1σ rms noise of the Q/U maps. The debiased polarization percentage P and its uncertainty δP are therefore derived by:

$$P = \frac{\text{PI}}{I}, \quad (3)$$

and

$$\delta P = \sqrt{\left(\frac{\sigma_{\text{PI}}^2}{I^2} + \frac{\sigma_I^2(Q^2 + U^2)}{I^4}\right)}, \quad (4)$$

where σ_I is the 1σ rms noise of the I map.

Finally, the polarization position angle θ and its uncertainty $\delta\theta$ (Naghizadeh-Khouei & Clarke 1993) are estimated to be:

$$\theta = \frac{1}{2} \tan^{-1}\left(\frac{U}{Q}\right), \quad (5)$$

and

$$\delta\theta = \frac{1}{2} \sqrt{\frac{\sigma_{Q/U}^2}{(Q^2 + U^2)}}. \quad (6)$$

3. Results

3.1. Dust Continuum

The 1.3 mm continuum emissions of three clumps are shown in Figure 2. In this subsection, we briefly overview the dust continuum emissions in MM4 and MM9, and focus on interpreting the dust continuum of MM1.

The MM4 region was studied by Zhang et al. (2015), Kong et al. (2018a), and Kong (2019), revealing six cores (MM4-Core1 to MM4-Core6 from northeast to southwest) along the natal filament and identifying the condensation-scale fragment structures in the continuum emission. We adopt the condensations identified by Zhang et al. (2015) and Kong (2019) in our study. In MM9, two massive dense cores, C1-N and C1-S, were identified by Tan et al. (2013). C1-S was further resolved into two protostellar condensations, C1-Sa and C1-Sb (Tan et al. 2016; Kong et al. 2018b). Due to sensitivity limitation, the two additional candidate protostellar sources, C1a and C1b

¹² <https://almascience.eso.org/observing/prior-cycle-observing-and-configuration-schedule>

Table 2
Observational Parameters

Date ^a	Configuration	N_{ant} ^b	Bandpass Calibrator	Gain Calibrator	Flux Calibrator	Pol Calibrator	Sources
2017 Apr 18	C40-3	48	J1751+0939	J1851+0035	Titan	J1751+0939	MM1, MM4, MM9
2018 Apr 29	C43-3	43	J1751+0939	J1851+0035	Titan	J1751+0939	MM1, MM4, MM9
2018 Jun 23	C43-1	47	J1751+0939	J1851+0035	J1751+0939	J1924-2914	MM4, MM9
2018 Jun 29	C43-1	45	J1751+0939	J1851+0035	J1751+0939	J1924-2914	MM4, MM9

Notes.

^a Observations were under precipitable water vapor (PWV) ranging from 1.3 to 2.1 mm.

^b Number of antennas.

(Tan et al. 2016), away from C1-N and C1-S are not detected in our ALMA 1.3 mm continuum.

The continuum emission of MM1 is resolved down to condensation scales (see Figure 2). The emission is dominated by a major core (hereafter MM1-Core1) in the west, which further fragments into several condensation structures. Several more condensations connected to the main core are detected in the east and in the southwest. Another strong condensation is seen to the northwest of the main core. There also appear to be two additional 6σ continuum peaks to the northeast and to the east of MM1-Core1.

To characterize the dense structures in MM1, we applied the dendrogram (Rosolowsky et al. 2008) technique on the dust continuum using the Python package *astrodendro*. The dendrogram abstracts the changing topology of the isosurfaces as a function of contour levels and tracks the hierarchical structure over a range of scales (Rosolowsky et al. 2008). This algorithm has three main parameters: the minimum value for the structure to be considered (*min_value*), the minimum height required for a structure to be retained as independent (*min_delta*), and the minimum number of pixels for a structure to be considered (*min_npix*). Following similar works (Cheng et al. 2018; Liu et al. 2018a), we adopt *min_value* = 4σ , *min_delta* = 1σ , and set *min_npix* to be the number of pixels in the half beam area. We note that the combination of *min_value* and *min_delta* ensures that the identified structures have peak fluxes $>5\sigma$.

The structures identified by dendrogram in MM1 are shown in Figure 3. The dendrogram reports the coordinates, the integrated flux (S_{int}), the FWHM sizes along the major and minor axes, and the position angles (θ_{dendro}) of the structures. The parameters derived by dendrogram are reported in Table 3. The brightest two sources, Condensation 1 and Condensation 2, correspond to P2-SMA1 and P2-SMA2 in Zhang et al. (2009). We note that nearly all condensations in MM1 are smaller than the beam area—except for Condensation 8, which is marginally resolved.

With the assumptions of the optically thin dust emission, isothermal, and a dust-to-gas ratio Λ of 1:100 (Beckwith & Sargent 1991), the gas mass M of the dense structures can be calculated with

$$M = \frac{\Lambda S_{\text{int}} d^2}{\kappa_{\nu} B_{\nu}(T)}, \quad (7)$$

where $d = 4.8$ kpc is the distance to G28.34, $\kappa_{\nu} = (\nu/1 \text{ THz})^{\beta}$ is the dust opacity (Hildebrand 1983) in $\text{m}^2 \text{kg}^{-1}$, and $B_{\nu}(T)$ is the Planck function at temperature T . Multiwavelength observations toward massive star-forming regions usually found dust emissivity indexes β of ~ 1.5 (Beuther et al. 2007;

Chen et al. 2007). Adopting this value, the κ_{ν} is estimated to be $0.11 \text{ m}^2 \text{kg}^{-1}$. The gas temperature map of the entire IRDC G28.34 was derived by Wang (2018) with combined VLA and Effelsberg 100 m data (Wang et al. 2008) of the NH_3 (1,1) and (2,2) lines at a resolution of $6''.5 \times 3''.6$. The temperatures of the condensations in MM1 range from 15 to 27 K. Considering that Condensation 1 is a hot molecular core (Zhang et al. 2009), the NH_3 (1,1) and (2,2) lines, which are cold gas tracers (Ho & Townes 1983), might have underestimated the gas temperature in this condensation. As a good approximation of dust heated by a central source with luminosity L_* , the dependence of dust temperature T on radius r behaves like a simple power law (Terebey et al. 1993):

$$T = T_0 \left(\frac{r}{r_0} \right)^{-q} \left(\frac{L_*}{L_0} \right)^{q/2}, \quad (8)$$

where T_0 is the fiducial dust temperature at a fiducial radius r_0 from a central source with luminosity L_0 and q is the power-law index. The luminosity of the embedded protostellar object in Condensation 1 is $L_* = 2950 L_{\odot}$ (Ragan et al. 2012). Adopting $T_0 = 38$ K, $r_0 = 100$ au, $q = 0.4$ (Motte & André 2001), and a background temperature of 20 K (Wang 2018), the average temperature of Condensation 1 within a radius of mean FWHM ($\text{FWHM}_{\text{mean}}$) is measured to be 57.0 K. A temperature of 30 K (Wang et al. 2008) is adopted for MM1-Core1. With a similar approach and adopting a temperature of ~ 16 K (Wang et al. 2008), we also derived the mass for MM4-Core4. The estimated masses and temperatures are listed in Table 3.

The average column density N_{H_2} and volume density n_{H_2} within each core and condensation are measured using a radius equal to the $\text{FWHM}_{\text{mean}}$:

$$N_{\text{H}_2} = \frac{M}{\mu_{\text{H}_2} m_{\text{H}} \pi \text{FWHM}_{\text{mean}}^2}, \quad (9)$$

$$n_{\text{H}_2} = \frac{3M}{4\mu_{\text{H}_2} m_{\text{H}} \pi \text{FWHM}_{\text{mean}}^3}, \quad (10)$$

where $\mu_{\text{H}_2} = 2.86$ is the mean molecular weight per hydrogen molecule (Kirk et al. 2013; Pattle et al. 2015) and m_{H} is the atomic mass of hydrogen. The derived column and volume densities are also listed in Table 3. The estimated n_{H_2} and N_{H_2} of the condensations in MM1 and the two cores ($n_{\text{H}_2} \sim 10^5$ – 10^7 cm^{-3} and $N_{\text{H}_2} \sim 10^{22}$ – 10^{24} cm^{-2}) are generally comparable to those in other IRDCs and in more evolved massive star-forming regions; see, e.g., Liu et al. (2018a), Lu et al. (2018), Cao et al. (2019), and Sanhueza et al. (2019). The main

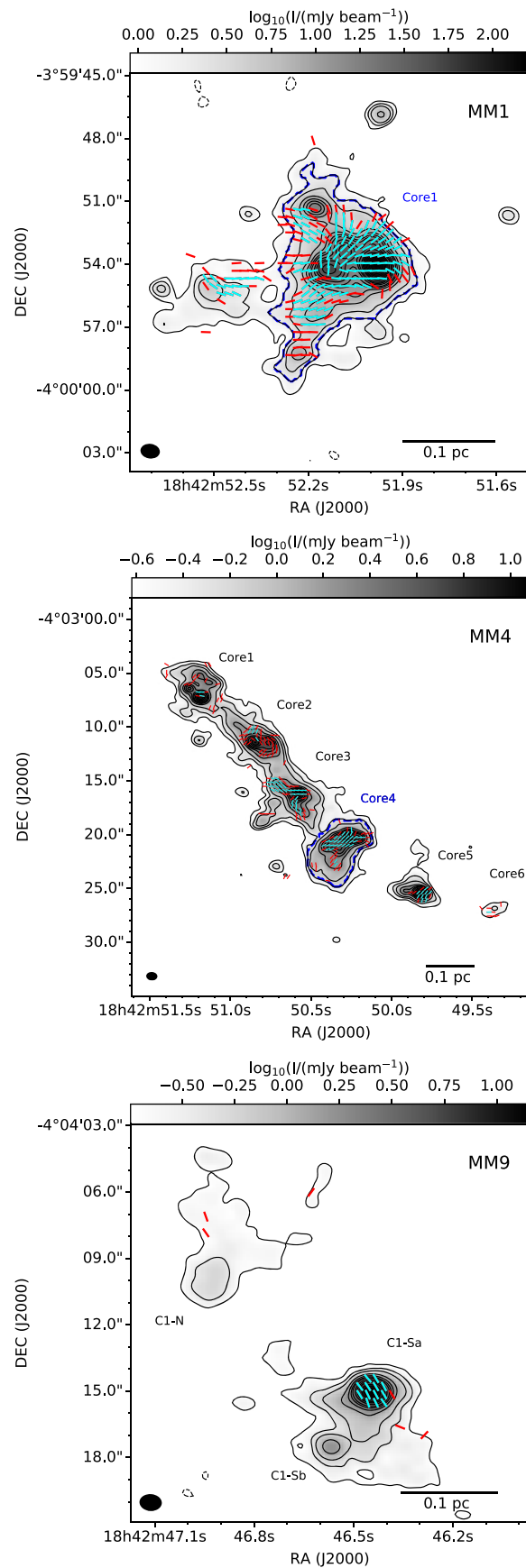


Figure 2. Dust continuum and magnetic orientation maps. Stokes I of the ALMA 1.3 mm continuum is shown in gray scales and in contours. ALMA 1.3 mm continua of three clumps are also shown in contours. Contour levels are $(\pm 3, 6, 10, 20, 30, 40, 50, 70, 90, 150, 180, 210, 250, 290, 340, 390, 450) \times \sigma_I$, where σ_I is the rms noise of the Stokes I maps (see Section 2). Line segments represent the orientation of the plane-of-sky magnetic field and have arbitrary length. Red and cyan line segments correspond to data with $PI/\sigma_{PI} > 2$ and $PI/\sigma_{PI} > 3$, respectively. Blue dashed regions indicate the areas of MM1-Core1 and MM4-Core4 in which the polarization data are used for the angular dispersion function analysis. The size of each synthesized beam is indicated in the lower left corner of each panel.

Table 3
Physical Parameters of Dense Structures

Source	R.A. (h:m:s)	Decl. (d:m:s)	$S_{\text{int}}^{\text{a}}$ (mJy)	FWHM ^b " × "	θ_{dendro} ($^{\circ}$)	T (K)	M (M_{\odot})	N_{H_2} (10^{23} cm^{-2})	N_{H_2} (10^6 cm^{-3})
MM1-Core1	18:42:52.06	-3:59:54.04	745.4	2.8×2.6	-138.8	30.0	212.4	5.0	3.2
Condensation 1	18:42:51.98	-3:59:54.06	258.0	0.8×0.6	126.2	57.0	35.5	>13.6	>29.2
Condensation 2	18:42:52.12	-3:59:54.23	57.7	0.6×0.4	177.8	23.6	21.9	>23.5	>56.5
Condensation 3	18:42:52.08	-3:59:53.41	25.0	0.4×0.3	97.0	23.6	9.5	>20.4	>65.6
Condensation 4	18:42:52.17	-3:59:51.35	26.8	0.7×0.5	159.5	24.1	9.9	>5.7	>11.8
Condensation 5	18:42:52.2	-3:59:58.24	9.7	0.6×0.5	53.9	17.3	5.5	>4.7	>11.0
Condensation 6	18:42:52.16	-3:59:56.16	9.8	0.7×0.4	-148.4	23.6	3.7	>4.0	>8.8
Condensation 7	18:42:51.96	-3:59:46.8	7.0	0.6×0.5	-155.7	15.2	4.7	>3.2	>8.8
Condensation 8	18:42:52.49	-3:59:55.26	12.2	1.1×0.7	170.7	21.9	5.1	>1.9	>2.5
Condensation 9	18:42:52.66	-3:59:55.19	2.8	0.5×0.4	156.2	17.7	1.6	>1.8	>5.2
Condensation 10	18:42:51.98	-3:59:57.14	2.2	0.5×0.4	149.3	26.4	0.7	>1.1	>2.8
Condensation 11	18:42:51.56	-3:59:51.66	1.5	0.4×0.3	154.8	20.2	0.7	>1.2	>4.2
Condensation 12	18:42:52.43	-3:59:56.17	1.4	0.4×0.3	158.5	19.4	0.7	>1.6	>5.4
Condensation 13	18:42:52.38	-3:59:51.5	0.9	0.4×0.3	161.6	19.8	0.4	>1.1	>4.2
Condensation 14	18:42:52.64	-3:59:56.81	1.2	0.6×0.2	179.3	17.7	0.6	>1.3	>3.9
Condensation 15	18:42:52.08	-3:59:58.52	1.7	0.7×0.3	176.0	21.1	0.7	>1.0	>2.6
MM4-Core4	18:42:50.31	-4:03:21.07	68.3	2.9×1.8	45.9	16.0	43.0	1.5	1.1

Notes.

^a Integrated flux.

^b Without deconvolution.

uncertainty of the calculations comes from the uncertainty of κ_{ν} (Henning et al. 1995). We conservatively adopt a fractional uncertainty of 50% (Roy et al. 2014) for M , N_{H_2} , and n_{H_2} . We note that, since most condensations are unresolved, the derived N_{H_2} and n_{H_2} for these condensations should be regarded as lower limits.

3.2. Polarized Emission of Dust

The plane-of-sky magnetic field orientation can be derived by rotating the orientation of the observed linear dust polarization of the electric field by 90° with the assumption that the shortest axis of dust grains is perfectly aligned with the magnetic field. Figure 2 shows the inferred magnetic field orientations overlaid on the Stokes I maps toward the massive clumps MM1, MM4, and MM9. The ALMA maps reveal compact structures in the clumps down to scales of ~ 0.02 pc (condensation scale).

The magnetic field structure in MM1 is well resolved and shows a radial pattern, indicating that the field might be dragged toward the center by gravity. We further compare the magnetic field with the local gravity in Section 3.6.

In MM4, strong polarized emissions are detected in MM4-Core3, MM4-Core4, and MM4-Core5, while the polarized emissions in MM4-Core1, MM4-Core2, and MM4-Core6 are only marginally detected. The polarized emission in Core5 is compact and centered at the continuum peak in the west of the core, showing a northwest–southeast oriented magnetic field that is orthogonal to the parent filament. The polarized emission in MM4-Core4 is the most extended in MM4 and the magnetic field in the northern part of this core is well resolved, while the magnetic field in the southern part is only partially resolved. Similar to Core5, the magnetic field in Core4 shows a northwest–southeast orientation. The magnetic field in Core3 can be divided into three groups: the magnetic field in the center shows a east–west orientation; the magnetic field

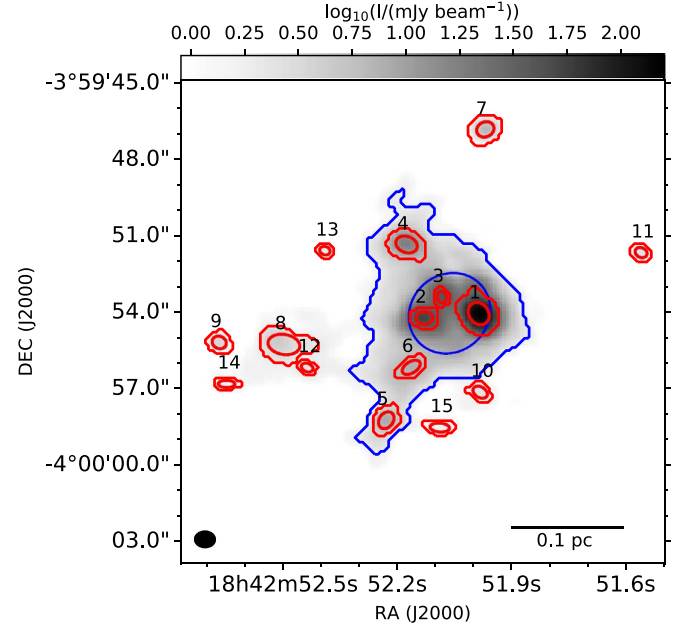


Figure 3. Structures identified by dendrogram in MM1. Gray scale shows the 1.3 mm continuum emission. Red and blue contours indicate the boundaries of the identified leaves (i.e., condensations) and MM1-Core1, respectively. Red and blue ellipses indicate the FWHM and position angle of the condensations and MM1-Core1, respectively, computed by dendrogram.

in the northeastern part shows a northeast–southwest orientation; and the magnetic field in the southern part rotates smoothly, showing a C-shaped morphology.

In MM9, the polarized emission is confined at the continuum peak (C1-Sa) and the magnetic field shows a northeast–southwest orientation, following the parent filament.

In Figure 4, we show contours of the polarization emission intensity overlaid on the polarization percentage maps. In

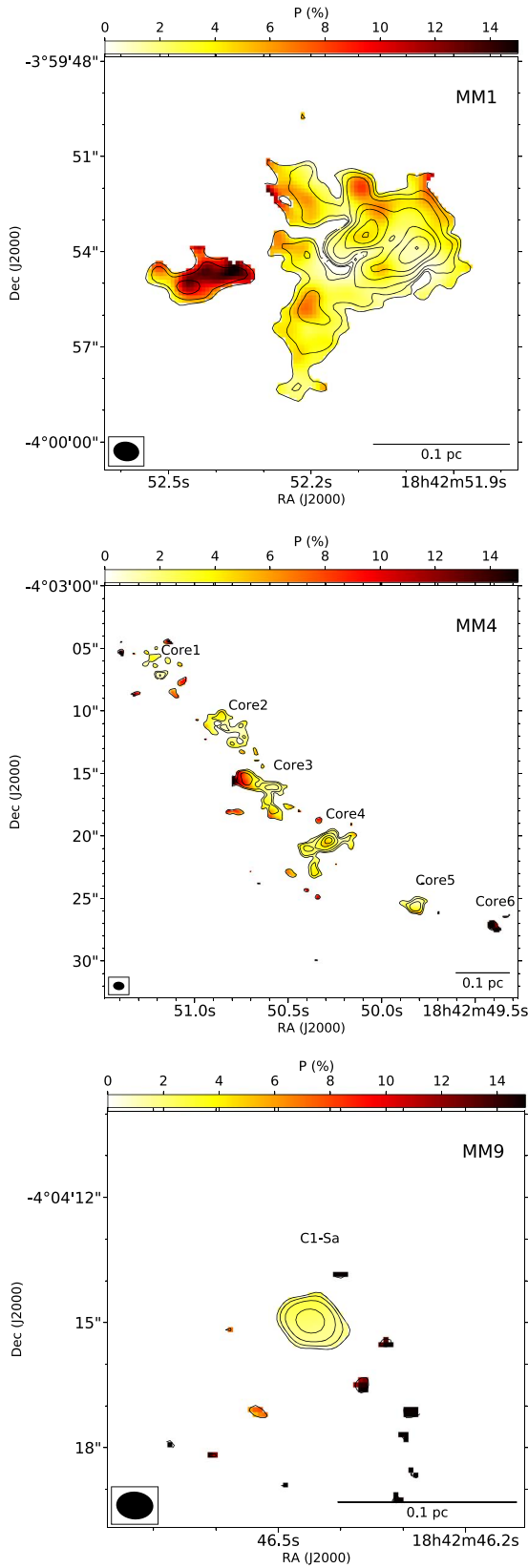


Figure 4. Dust polarization maps. The polarization percentage is shown in color scale. Black solid contours show the polarized intensity. Contour levels are (2, 3, 5, 10, 15, 25, 35, 50) $\times \sigma_{PI}$, where σ_{PI} is the rms noise of the polarized intensity ($\sim 50 \mu\text{Jy}/\text{beam}$ for MM1 and $\sim 20 \mu\text{Jy}/\text{beam}$ for MM4 and MM9). Gray dashed contours show the dust continuum emission with the same contour levels as those in Figure 2, but only the positive levels are drawn.

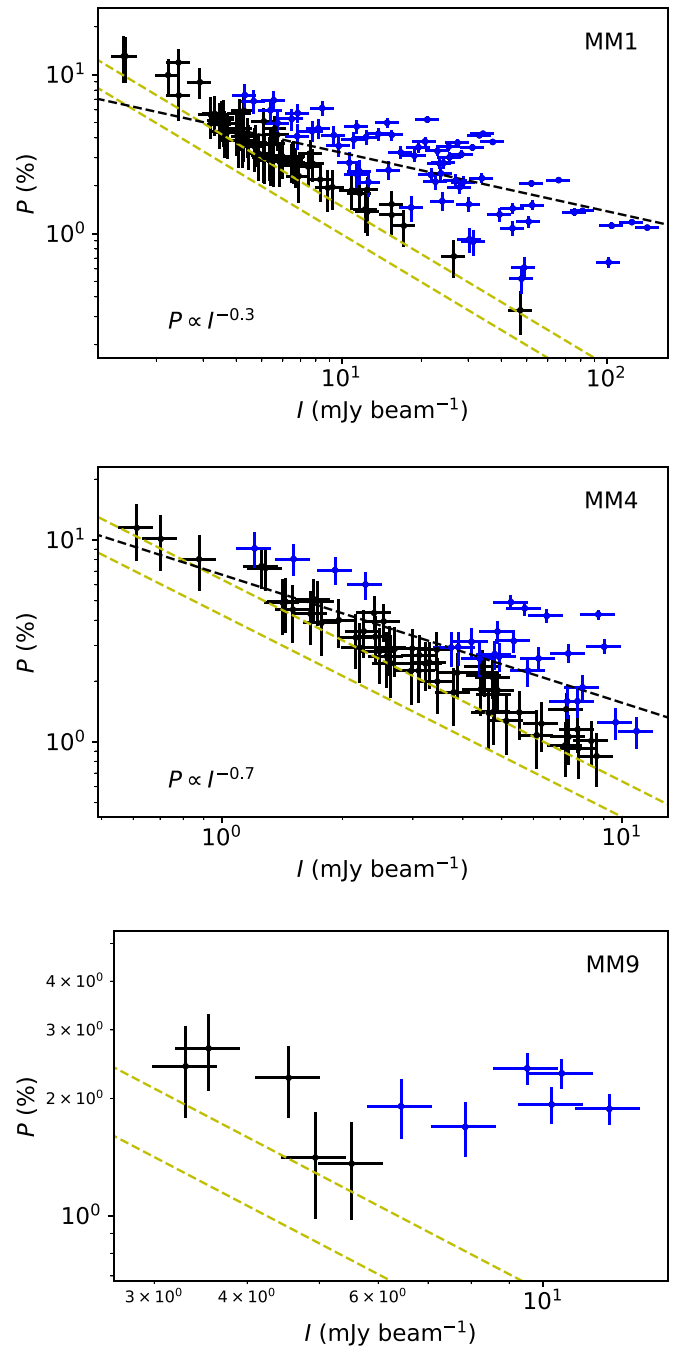


Figure 5. Polarization percentage vs. Stokes I . Data points with $P/\delta P > 3$ and $P/\delta P > 5$ are shown with error bars in black and blue colors, respectively. Yellow dashed lines show the $2\sigma_{PI}$ and $3\sigma_{PI}$ noise levels. Results of the power-law fit for data with $P/\delta P > 3$ are shown in black dashed lines.

Figure 5, the P - I relation in the three clumps is shown. The polarization percentage is detected down to 0.3%, 0.8%, and 1.3% in MM1, MM4, and MM9, respectively. Clear trends of decreasing P with increasing I are seen in MM1 and MM4. For the P - I relations in MM1 and MM4, the polarization percentage at a constant I shows broad scatters up to an order of magnitude, which indicates that the depolarization seen in the two clumps are the combined results of different factors. Using χ^2 minimization, we fit the P - I anticorrelations in MM1 and MM4, where $P/\delta P > 3$ with a simple power-law $P \propto I^\alpha$

and the power-law slope index α is estimated to be approximately -0.3 and -0.7 for MM1 and MM4, respectively. Due to the large scattering in the $P-I$ relations, we refrain from interpreting the absolute value of the slope indexes. However, we notice that the $P-I$ relation in MM1 is shallower than that in MM4, which may suggest the grain alignment efficiency is improved by additional internal radiation in more evolved star formation regions. A similar trend of shallower $P-I$ relations in more evolved cores is also seen in the low-mass star formation dense cores in the Ophiuchus cloud (Kwon et al. 2018; Soam et al. 2018; Liu et al. 2019; Pattle et al. 2019). In MM9, the polarized percentage is $\sim 2\%$.

3.3. Molecular Lines

Figure 6 show the zeroth-moment maps of N_2D^+ (3-2), ^{13}CS (5-4), and OCS (19-18) in MM1, MM4, and MM9. The line emissions in three clumps share some similar patterns. The ^{13}CS and OCS lines show similar emission morphology and present the strongest emission mostly near the dust continuum peaks. The distribution of the N_2D^+ emission is almost anticorrelated with that of the ^{13}CS and OCS emission, indicating that the ^{13}CS and OCS molecules are likely depleted in the cold and dense gas highlighted by the N_2D^+ emission.

In MM1, the emissions from ^{13}CS and OCS peak at Condensation 1. The N_2D^+ line shows strong emissions to the north of Core1, which appears to be extended and probably links Condensation 7 with MM1-Core1. There are also faint N_2D^+ emissions in Condensation 10 and between Condensations 5 and 6. The lack of N_2D^+ detection in the dust emission region indicates that MM1 is in a later evolution stage of star formation.

In MM4, the N_2D^+ emission is detected in MM4-Core1 through Core5, while the ^{13}CS and OCS emissions are detected in MM4-Core1 through Core4. The line emission of three molecules are mostly overlapping with dust continuum emissions, except that there appears to be an N_2D^+ emission peak to the east of MM4-Core1 and an OCS emission peak to the south of MM4-Core1, neither of which is associated with the dust emission above 3σ . The ^{13}CS and N_2D^+ maps generally agree with previous observations reported in Zhang et al. (2015), but show improvements in detecting fainter and more extended emissions.

In MM9, the ^{13}CS and OCS emissions are only marginally detected in C1-S. The N_2D^+ emission in core C1-S are consistent with previous observations (Tan et al. 2013, 2016; Kong et al. 2018b). Due to the limitation of sensitivity, the N_2D^+ emission in core C1-N is only marginally detected.

3.4. Molecular Outflows in MM1

The molecular outflows in MM4 (Wang et al. 2011; Zhang et al. 2015) and MM9 (Feng et al. 2016a; Tan et al. 2016; Kong et al. 2018b) have been widely studied, so we only present the outflows of MM1 in CO (2-1) in this paper (see Figure 7). The outflow emissions in MM1 are detected throughout the velocity coverage of our observations (~ 41 to ~ 116 km s^{-1}). Figure 7(a) shows the integrated emissions of CO in velocity ranges from 45 to 74 km s^{-1} for the blueshifted lobe, and 84–115 km s^{-1} for the redshifted lobe. The data channels with velocities < 84 and > 115 km s^{-1} are excluded in the integration in order to avoid the contamination of surrounding diffuse gas.

We also excluded channels with velocities < 45 or > 115 km s^{-1} in the integration, due to domination of instrumental noise in these edge channels. Figure 7(b) shows the integrated emission of the high-velocity (HV) outflow gas with velocities > 20 km s^{-1} with respect to MM1's ambient velocity. The outflows in MM1 show clustered overlapping structures. The HV outflow components are highly collimated and show some jet-like structures. Due to the complex structure of the outflows and the lack of shock tracers (e.g., SiO) to trace the vicinity outflow gas, we refrain from detailed analysis of the MM1 outflow and leave it to future studies.

3.5. Magnetic Field Strength of MM1-Core1 and MM4-Core4

The Davis–Chandrasekhar–Fermi (DCF; Davis 1951; Chandrasekhar & Fermi 1953) method and its modified form have been widely used to estimate the plane-of-sky magnetic field strength (B_{pos}) by interpreting the observed angular dispersion ($\Delta\theta$) of polarization position angles as an MHD-wave component of the field perturbed by turbulent motions. With the small angle approximation, the B_{pos} is estimated as (Crutcher et al. 2004):

$$B_{\text{pos}} = Q_c \sqrt{\mu_0 \rho} \frac{\sigma_{\text{turb}}}{\Delta\theta} \quad (11)$$

in SI units or CGS units, where μ_0 is the permeability of vacuum, $\rho = \mu_{\text{H}_2} m_{\text{H}} n_{\text{H}_2}$ is the density of the gas, σ_{turb} is the line-of-sight nonthermal velocity dispersion, and Q_c is a correction factor.

Further approaches have been made to modify the DCF method toward more accurately quantifying the angular dispersion in the DCF formula through the angular dispersion function (ADF) analysis (Falceta-Gonçalves et al. 2008; Hildebrand et al. 2009; Houde et al. 2009, 2016) or the unsharp masking analysis (Pattle et al. 2017). Specifically, Houde et al. (2016) derived the ADF for polarimetric images obtained from an interferometer, taking into account variations in the large-scale magnetic field, the effects of signal integration along the line of sight and within the beam, and the large-scale filtering effect of interferometers. The ADF is given by Houde et al. (2016):

$$1 - \langle \cos[\Delta\Phi(l)] \rangle = \sum_{j=1}^{\infty} a_{2j} l^{2j} + \left[\frac{N}{1 + N \langle B_0^2 \rangle / \langle B_t^2 \rangle} \right] \times \left\{ \frac{1}{N_1} [1 - e^{-l^2/2(\delta^2 + 2W_1^2)}] + \frac{1}{N_2} [1 - e^{-l^2/2(\delta^2 + 2W_2^2)}] - \frac{2}{N_{12}} [1 - e^{-l^2/2(\delta^2 + W_1^2 + W_2^2)}] \right\}. \quad (12)$$

Here, $\Delta\Phi(l)$ is the angular difference of two line segments separated by a distance l , δ is the turbulent correlation length, the summation is the Taylor expansion of the ordered component of the ADF, B_t is the turbulent component of the magnetic field, B_0 is the ordered magnetic field, W_1 and W_2 are the standard deviation of the two Gaussian profiles of the synthesized beam and the large-scale filtering effect (i.e., the FWHM divided by $\sqrt{8 \ln 2}$), and N is the number of turbulent

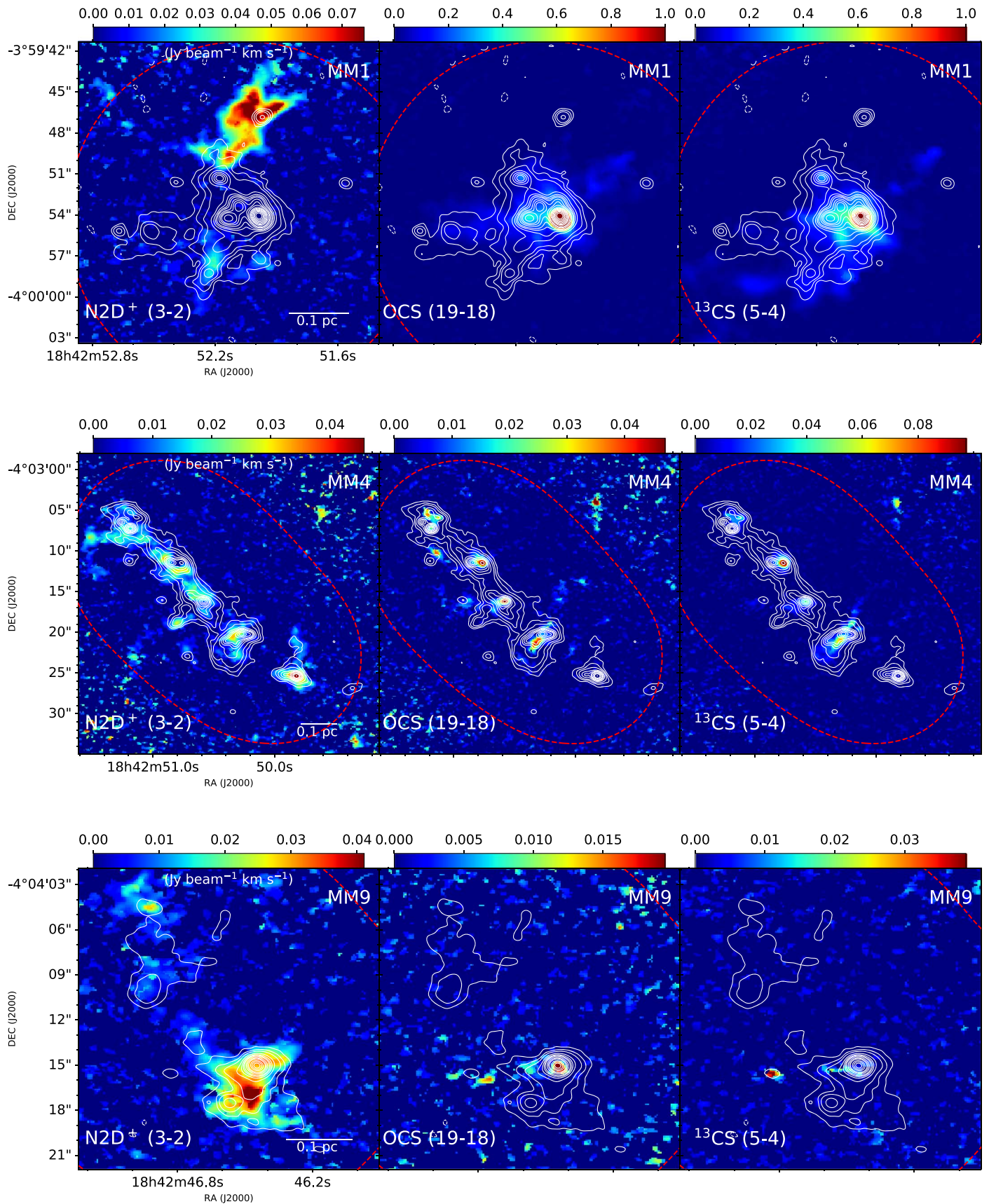


Figure 6. Moment 0 maps of molecular lines from N_2D^+ (3-2), ^{13}CS (5-4), and OCS (19-18) are shown in color scales. Only velocities with detection greater than 2σ rms noise are integrated. White contour levels are the same as the contour levels in Figure 2. Red contours correspond to the FWHM field of view of the ALMA observations.

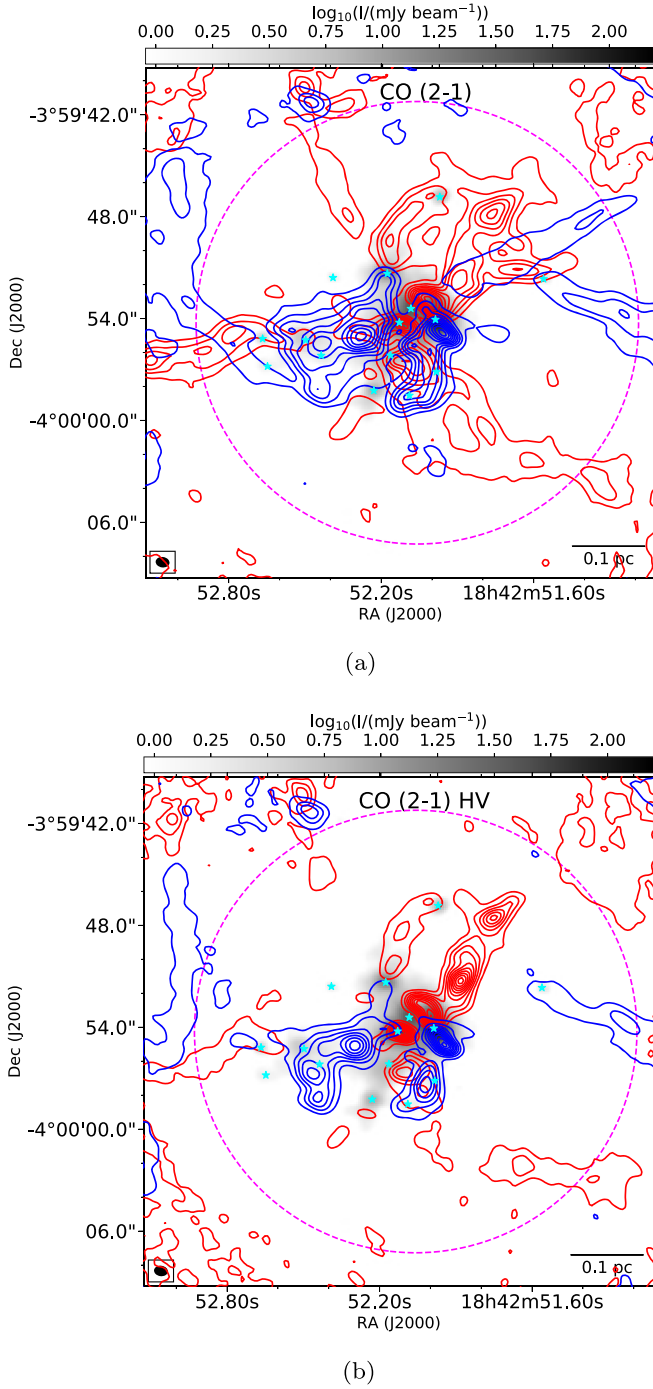


Figure 7. Molecular outflows detected in CO (2-1) in MM1. The blueshifted and redshifted outflows are shown in blue and red contours, respectively. Contour levels start from 5% and continue at 10% of the peak of the integrated CO emission. The dust continuum is shown in gray scale. Star symbols denote the position of the condensations identified by dendrogram. Magenta contours correspond to the FWHM field of view of the ALMA observations. (a) CO emissions integrated from 45 to 74 km s⁻¹ for the blue robe, and 84–115 km s⁻¹ for the red robe. (b) High-velocity (outflow velocity > ± 20 km s⁻¹) CO emissions integrated from 45 to 59 km s⁻¹ for the blue robe, and 99 to 115 km s⁻¹ for the red robe.

cells probed by the telescope beam, given by:

$$N_1 = \frac{(\delta^2 + 2W_1^2)\Delta'}{\sqrt{2\pi}\delta^3}, \quad (13)$$

$$N_2 = \frac{(\delta^2 + 2W_2^2)\Delta'}{\sqrt{2\pi}\delta^3}, \quad (14)$$

$$N_{12} = \frac{(\delta^2 + W_1^2 + W_2^2)\Delta'}{\sqrt{2\pi}\delta^3}, \quad (15)$$

$$N = \left(\frac{1}{N_1} + \frac{1}{N_2} - \frac{2}{N_{12}} \right)^{-1}, \quad (16)$$

where Δ' is the effective thickness of the concerned region through which the signals are integrated along the line of sight. The turbulent component of the ADF is

$$b^2(l) = \left[\frac{N}{1 + N \langle B_0^2 \rangle / \langle B_t^2 \rangle} \right] \times \left[\frac{1}{N_1} e^{-l^2/2(\delta^2 + 2W_1^2)} + \frac{1}{N_2} e^{-l^2/2(\delta^2 + 2W_2^2)} - \frac{2}{N_{12}} e^{-l^2/2(\delta^2 + W_1^2 + W_2^2)} \right].$$

The ordered magnetic field strength can be derived by (Houde et al. 2009):

$$B_0 \simeq \sqrt{\mu_0 \rho} \sigma_{\text{turb}} \left[\frac{\langle B_t^2 \rangle}{\langle B_0^2 \rangle} \right]^{-1/2} \quad (17)$$

in SI units or CGS units.

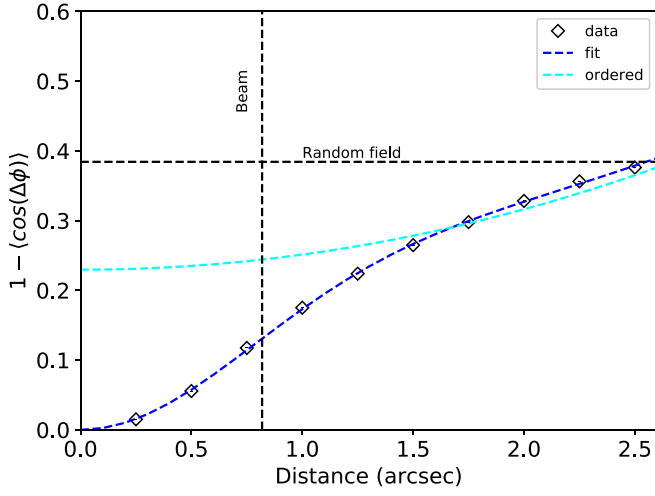
The Δ' is estimated as the width at half of the maximum of the normalized auto-correlation function of the integrated normalized polarized flux (Houde et al. 2009). The Δ' of MM1-Core1 and MM4-Core4 are estimated to be 2''5 and 2''2, respectively, values that are consistent with the FWHMs derived from dendrogram.

Information about the nonthermal (turbulent) velocity dispersion (σ_{turb}) of the gas, which is required to calculate the B_{pos} , is determined from previous NH₃ observations. The line-of-sight velocity dispersions of NH₃ (σ_{NH_3}) for MM1-Core1 and MM4-Core4 are 1.4 km s⁻¹ (Wang et al. 2008) and 0.47 km s⁻¹ (Wang et al. 2012), respectively. The σ_{turb} is calculated with the relation

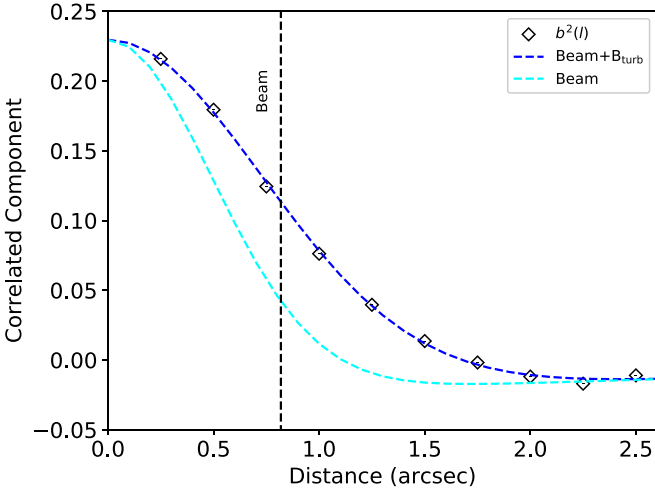
$$\sigma_{\text{turb}}^2 = \sigma_{\text{NH}_3}^2 - \frac{k_B T}{m_{\text{NH}_3}}, \quad (18)$$

where m_{NH_3} is the mass of the NH₃ molecule. The nonthermal velocity dispersions are estimated to be 1.4 km s⁻¹ and 0.46 km s⁻¹ for MM1-Core1 and MM4-Core4, respectively. The corresponding 3D turbulent velocity dispersions $\sigma_{\text{turb},3\text{D}} = \sqrt{3} \sigma_{\text{turb}}$ are 2.42 km s⁻¹ and 0.80 km s⁻¹ for MM1-Core1 and MM4-Core4, respectively.

Figures 8 and 9 show the ADFs and the turbulent component of the ADF derived from the polarization segments with $\text{PI}/\sigma_{\text{PI}} > 3$ in MM1-Core1 and MM4-Core4 (see Figure 2), respectively. To avoid large uncertainties due to sparse sampling at large spatial scales (see Appendix of Liu et al. 2019), we fit the ADFs of MM1-Core1 and MM4-Core4 over $l < 2''6$ and $l < 3''4$, respectively, where the ADF is relatively smooth and shows well-correlated relations with l . The best fit is obtained via χ^2 minimization. The B_{pos} for MM1-Core1 and MM4-Core4 are calculated to be 1.6 mG and 0.32 mG, respectively. The parameters derived from the ADF method are listed in Table 4. We note that, since the polarization observations in MM4-Core4 only cover part of this core, an assumption of constant turbulent-to-ordered magnetic field



(a)



(b)

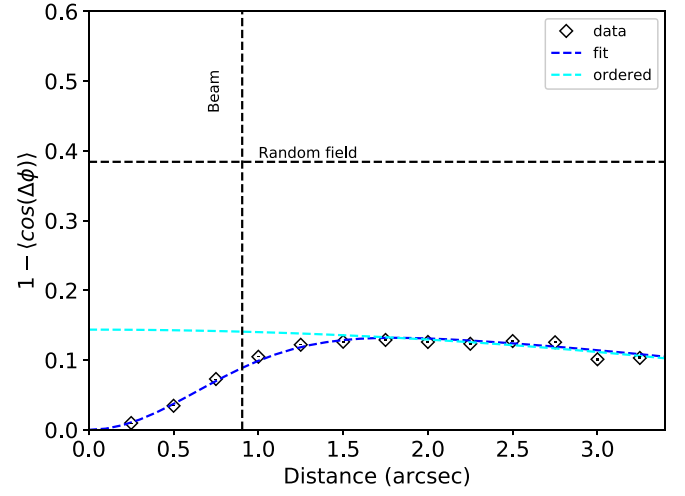
Figure 8. (a) Angular dispersion function for MM1-Core1. Angle dispersion segments are shown in diamond symbols with error bars. Error bars indicate the statistical uncertainties of the angular dispersion function propagated from the observational uncertainty. Blue dashed line shows the fitted ADF. Cyan dashed line shows the large-scale component ($1 - \langle \cos[\Delta\Phi(l)] \rangle - b^2(l)$) of the best fit. Horizontal dashed line indicates the value corresponding to a random field. (b) Correlated component ($b^2(l)$) of the ADF. The correlated component of the best fit is shown in the blue dashed line. The correlated component solely due to the beam is shown in the cyan dashed line.

ratio in the core needs to be adopted. According to Houde et al. (2016), the B_{pos} estimated from the ADF method is accurate within a factor of ~ 3 .

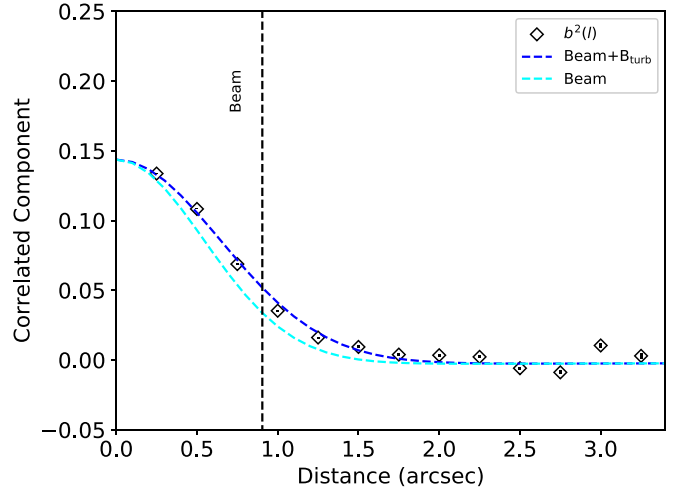
Since the line-of-sight component of the magnetic field is unknown, the 3D mean ordered magnetic field strength B is calculated with the statistical relation $B = 4B_{\text{pos}}/\pi$ (Crutcher et al. 2004). The 3D Alfvén velocity is then estimated as

$$V_{A,3D} = \frac{B}{\sqrt{\mu_0 \rho}} \quad (19)$$

in SI units or CGS units. The $V_{A,3D}$ for MM1-Core1 and MM4-Core4 are 1.5 km s^{-1} and 0.51 km s^{-1} , respectively. The Alfvén Mach number $\text{Mach}_A = \sigma_{\text{turb},3D}/V_{A,3D}$ of MM1-Core1 and MM4-Core4 are estimated to be 1.61 and 1.57,



(a)



(b)

Figure 9. Same as Figure 8 but for MM4-Core4.

respectively, which means that the two cores are in super-Alfvénic states (weakly magnetized).

3.6. Comparison of Orientations of Magnetic Field, Intensity Gradient, and Local Gravity

Star-forming regions are subject to various forces, such as gravity, gas pressure, magnetism, and other possible forces. Koch et al. (2012) has used ideal magnetohydrodynamics (MHD) force equations to describe the interaction of the forces and developed a technique (the polarization–intensity gradient–local gravity method, hereafter the PIL method) to measure the local magnetic field strength. In this method, the gradient of intensity is assumed to trace the resulting direction of particle motion in the MHD force equation. Following the approach of the PIL method, we calculate the angular differences among the magnetic field, the intensity gradient, and the local gravity, and study the relative importance of the magnetic field local gravity at different positions.

The surrounding mass distribution needs to be taken into account when calculating the local gravitational force at a given

Table 4
Physical Parameters Relevant to the ADF Analysis

Source	n_{H_2} (10^6 cm^{-3})	σ_{turb} (km s^{-1})	$(\langle B_t^2 \rangle / \langle B_0^2 \rangle)^{1/2}$	B_{pos} (mG)	δ ($^\circ$)	N	Q_c^{a}
MM1-Core1	3.2	1.4	1.2	1.6	0.53	4.1	0.50
MM4-Core4	1.1	0.46	1.2	0.32	0.38	6.9	0.38

Note.

^a Equivalent correction factor $Q_c' = 1/\sqrt{N}$ for the signal-integration effect.

position in a map (Koch et al. 2012). Adopting constant temperatures for MM4 and MM9, and adopting the previously mentioned temperature profile (see Section 3.1) for MM1, we derived the gas mass (m_i) for each pixel of the map with $I > 3\sigma_I$ for the three clumps using Equation (7). The local gravity force at position \mathbf{r}_j is then given by

$$\mathbf{g}_j(\mathbf{r}) = G \sum_{i=1}^n \frac{m_i m_j}{|\mathbf{r}_j - \mathbf{r}_i|^2} \mathbf{e}_{ij}, \quad (20)$$

where \mathbf{e}_{ij} is the direction between position \mathbf{r}_i and \mathbf{r}_j . The orientations of the local gravity force (θ_{LG}) of the three clumps are presented in Figure 10. The local gravity orientation maps show similar radial patterns toward local emission peaks, which is quite reasonable because the emission centers contain more mass and have larger gravitational potential.

3.6.1. Intensity Gradient versus Local Gravity

The angle ψ measures the angular difference between the position angles of the intensity gradient (θ_{IG}) and that of the local gravity (θ_{LG}). Figure 11 shows the ψ maps for the three clumps. The average values of ψ in MM1, MM4, and MM9 are 30° , 22° , and 28° , respectively. The small average value of ψ indicates that the intensity gradient tend to be aligned with the local gravity and that the gravity plays an important role in regulating the gas motion. On the other hand, there seem to be large ψ values near some condensations where accretion or rotation are likely ongoing.

3.6.2. Magnetic Field versus Intensity Gradient

The angle δ measures the angular difference between the position angles of the intensity gradient (θ_{IG}) and that of the magnetic field (θ_{B}). Figure 12 shows the δ maps for MM1 and MM4. The average values of δ in MM1 and MM4 are 40° and 46° , respectively. The intermediate average values of δ suggests that the magnetic field plays a moderate role in resisting the gas collapse.

3.6.3. Magnetic Field versus Local Gravity

The angle ω measures the angular difference between the position angles of the local gravity (θ_{LG}) and that of the magnetic field (θ_{B}). Figure 13 shows the ω maps for MM1 and MM4. The average values of ω in MM1 and MM4 are 34° and 36° , respectively. In both MM1 and MM4-Core4, the magnetic field and the local gravity are apparently poorly aligned toward the brightest emission peaks, which might be a result of field tangling of the complex small-scale magnetic field along the line of sight or the perturbation from rotation and accretion. In MM1, the well-aligned magnetic field and local gravity in the northwestern region suggest that the magnetic field morphology is shaped by gravity in this region, while the magnetic

field and the local gravity in the southwestern region are poorly aligned, suggesting that the magnetic field has kept its own dynamics.

If the hydrostatic gas pressure is negligible, the local ratio between magnetic field force F_{B} and the gravity force F_{G} can be measured by the magnetic field-to-gravity force ratio (Koch et al. 2012)

$$\Sigma_{\text{B}} = \frac{\sin \psi}{\sin(90^\circ - \delta)} = \frac{F_{\text{B}}}{|F_{\text{G}}|}. \quad (21)$$

Figure 14 shows the Σ_{B} maps for MM1 and MM4. The median values of Σ_{B} in MM1 and MM4 are 0.47 and 0.27 respectively. The small values of Σ_{B} indicate that, overall, the magnetic field cannot solely balance the gravitational force.

4. Discussion

4.1. Uncertainty of the DCF Method for Super-Alfvénic Cases

The accuracy of the DCF method has been under investigation in the literature. The reliability of the DCF method can be tested with numerical simulations (Heitsch et al. 2001; Ostriker et al. 2001; Padoan et al. 2001; Falceta-Gonçalves et al. 2008). Specifically, Heitsch et al. (2001) and Falceta-Gonçalves et al. (2008) investigated the effect of large angular dispersion and the effect of energy equipartition between the turbulent magnetic energy and the turbulent kinetic energy. Their results showed that the DCF method could overestimate the magnetic field strength for super-Alfvénic models.

The equipartition between the turbulent magnetic energy and the turbulent kinetic energy is a basic assumption of the DCF method. However, since the perturbation on the magnetic field cannot follow the strong kinetic motions for super-Alfvénic cases, the energy equipartition would be broken and the magnetic field strength would be overestimated (Heitsch et al. 2001; Falceta-Gonçalves et al. 2008).

Another basic assumption of the DCF method is that the dispersion of polarization position angles corresponds to the ratio between the turbulent and ordered components of the magnetic field. For weak fields with Alfvén Mach number > 1 , the magnetic field lines can easily be distorted and the angular dispersion can approach that expected for a random field. As a consequence, the measured angular dispersion cannot reflect the true extent of the perturbed magnetic field and the magnetic field strength would be overestimated (Heitsch et al. 2001; Falceta-Gonçalves et al. 2008).

The magnetic field strength of MM1-Core1 and MM4-Core4 is derived from the ADF method (see Section 3.5). The ADF method improves the original DCF method by taking into account the signal-integration effect and the large-scale field. However, the ADF method does not correct for the aforementioned effects of energy equipartition and large angular dispersion. Since the two cores are in super-Alfvénic states (see

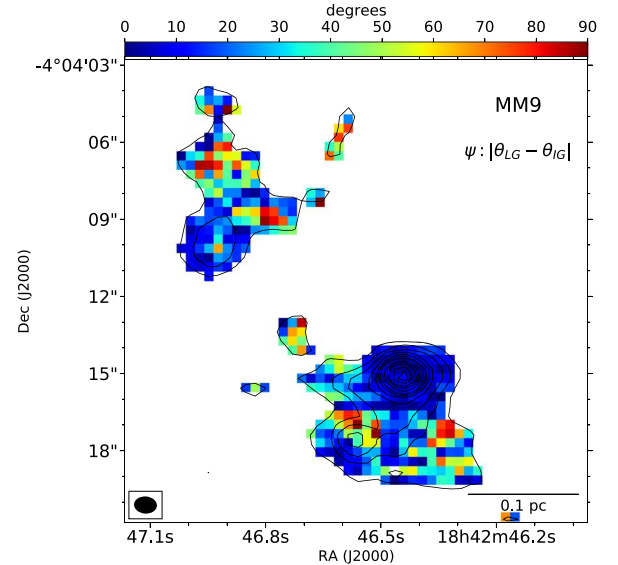
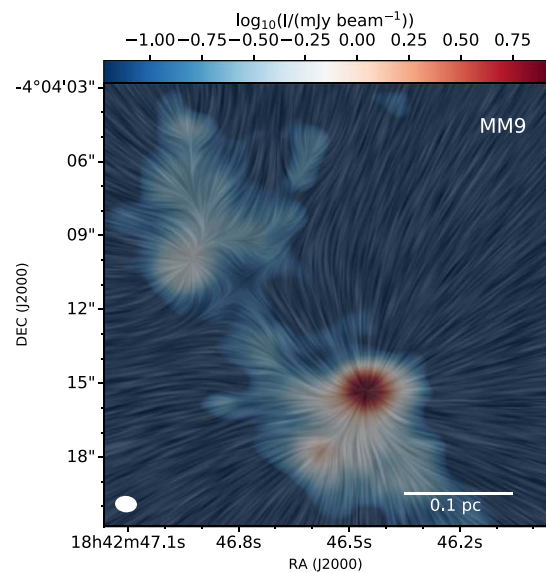
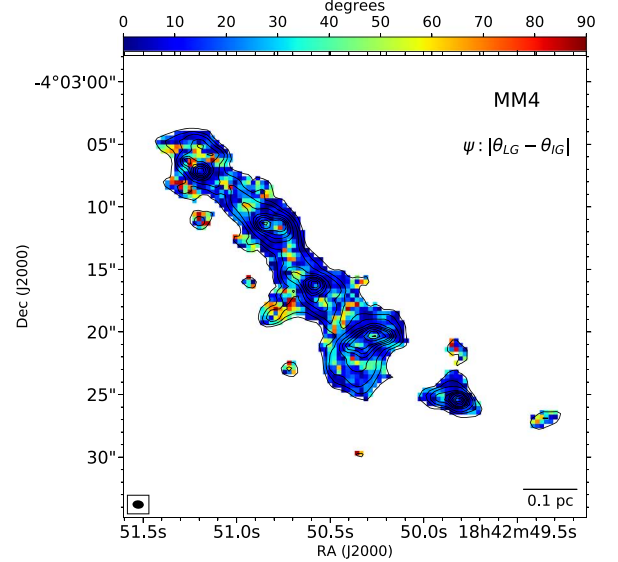
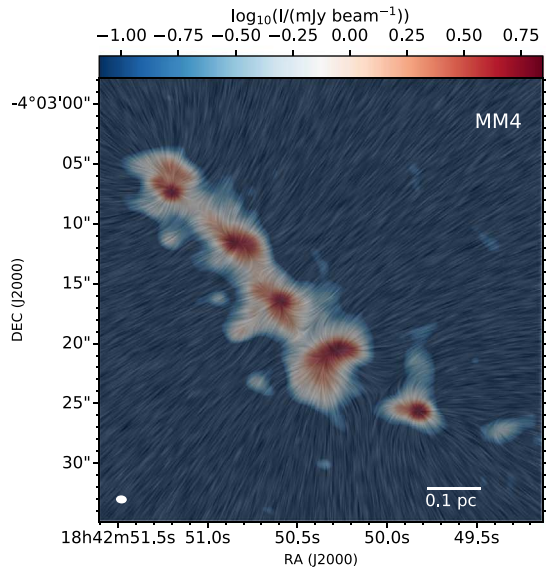
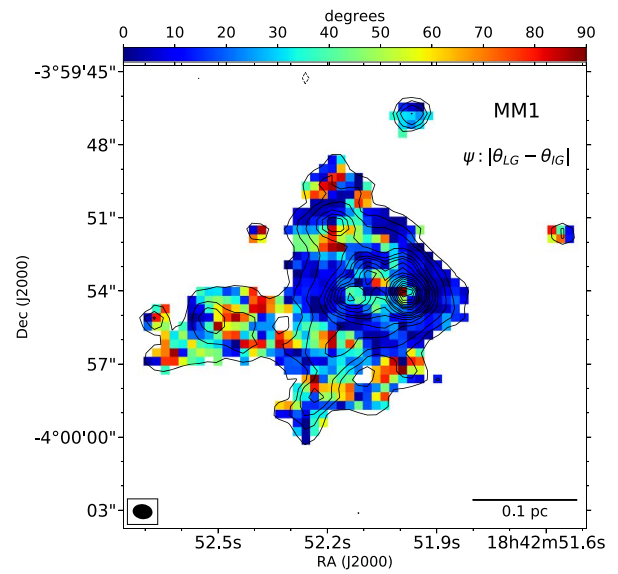
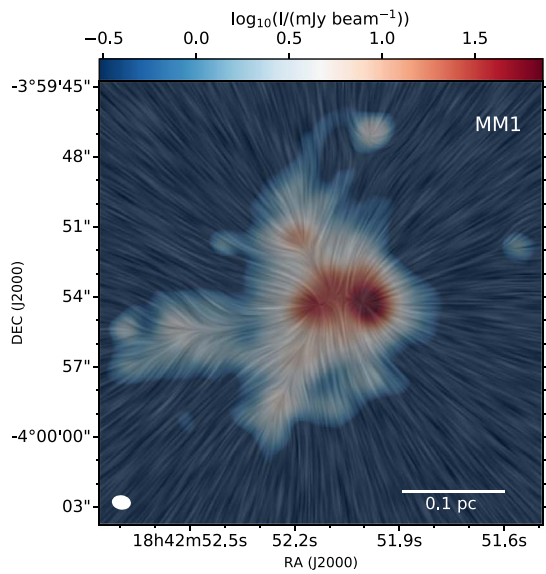


Figure 10. Local gravity orientation maps. Stokes I of the ALMA 1.3 mm continuum is shown in color scale. Overlaid patterns are produced with the line integral convolution method (LIC; Cabral & Leedom 1993) and indicate the orientation of the local gravity (θ_{LG}).

Figure 11. Angle differences between orientations of the intensity gradient and the local gravity ($\psi = |\theta_{IG} - \theta_{LG}|$). Contour levels are the same as those in Figure 2.

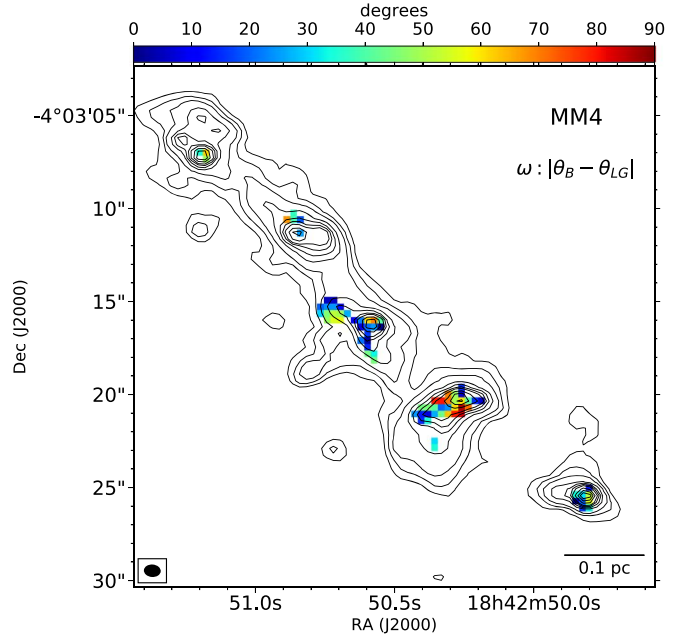
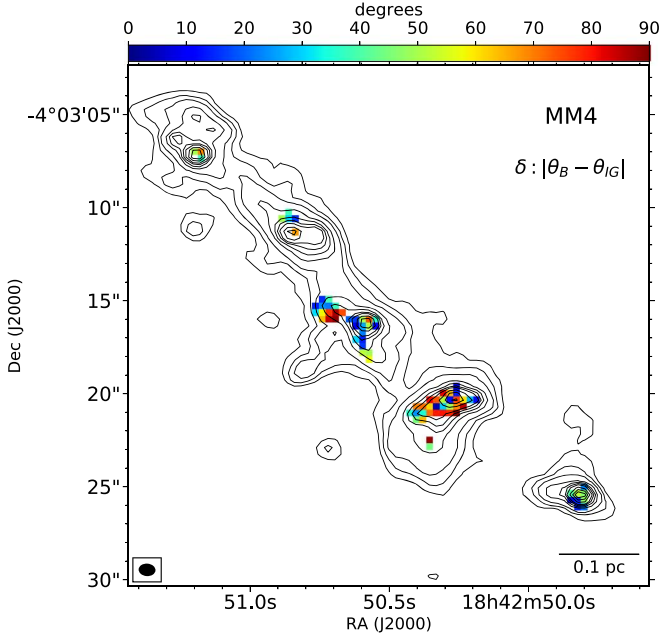
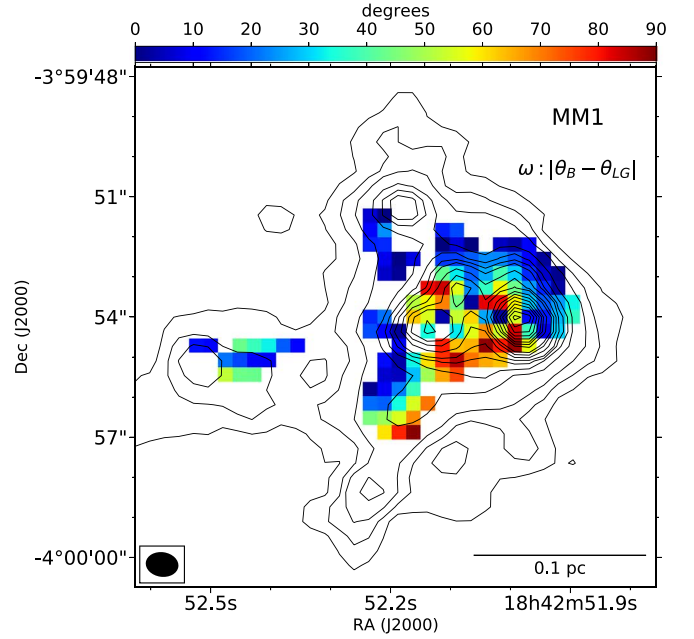
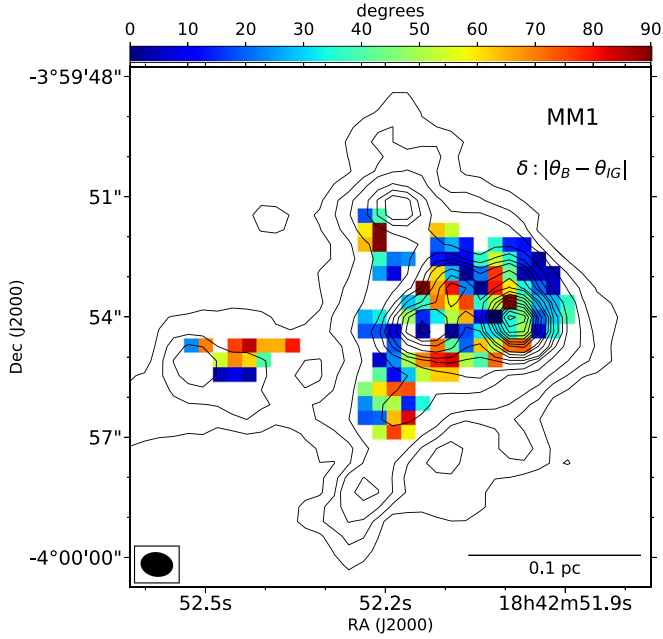


Figure 12. Angle differences between orientations of the magnetic field and the intensity gradient ($\delta = |\theta_B - \theta_{IG}|$). Values of δ are computed at where $PI/\sigma_{PI} > 3$. Contour levels are the same as those in Figure 2.

Figure 13. Angle difference between orientations of the magnetic field and the local gravity ($\omega = |\theta_B - \theta_{LG}|$). Values of ω are computed where $PI/\sigma_{PI} > 3$. Contour levels are the same as those in Figure 2.

Section 3.5), it is possible that the ADF method has overestimated the magnetic field strength in the two cores.

4.2. Dynamical State

The star formation process are governed by the complex interplay of self-gravity and competing processes (e.g., turbulence, thermal pressure, magnetic fields, stellar feedback, and rotation). For decades, the virial theorem has been used to study whether star-forming regions are stable against gravitational collapse. We briefly review the concept of the virial theorem and point out possible mistakes in some previous virial studies in Appendix. Here, we calculate the relevant parameters

in MM1-Core1 and MM4-Core4, and discuss the implication on massive star formation.

4.2.1. Dynamic States in MM1-Core1 and MM4-Core4

We computed the virial masses and virial parameters for the two massive dense cores MM1-Core1 and MM4-Core4. The thermal velocity dispersion (1D sound speed, σ_{th}) is derived by

$$\sigma_{th} = \sqrt{\frac{k_B T}{\mu_p m_H}}, \quad (22)$$

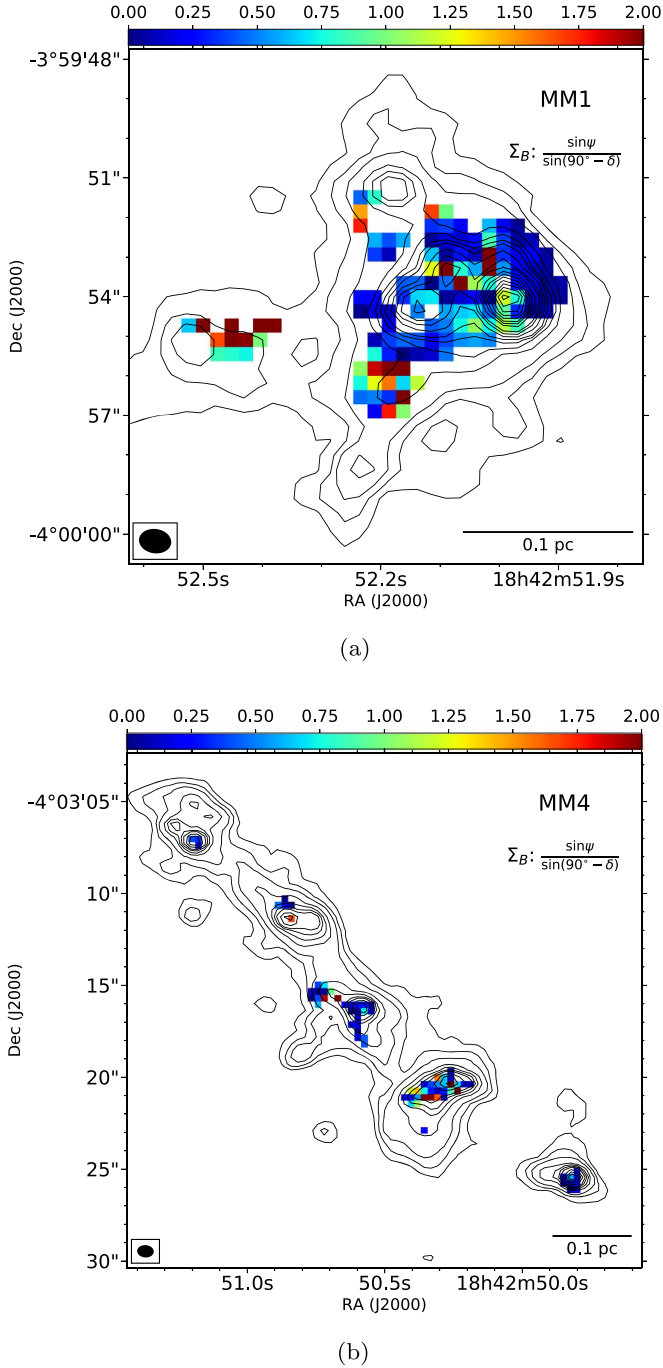


Figure 14. Maps of Σ_B . Values of Σ_B are computed where $PI/\sigma_{PI} > 3$. Contour levels are the same as those in Figure 2.

where $\mu_p = 2.33$ is the conventional mean molecular weight per free particle. The 3D sound speed is estimated as $\sigma_{th,3D} = \sqrt{3}\sigma_{th}$. We adopted respective radial density profiles $\rho \propto r^{-a}$ of $a = 1.6$ and $a = 2.1$ for MM1-Core1 and MM4-Core4 (Zhang et al. 2009). The kinetic virial mass is derived by

$$M_k = \frac{3(5 - 2a)\sigma_{tot}^2 R}{(3 - a)G}, \quad (23)$$

where $\sigma_{tot} = \sqrt{\sigma_{th}^2 + \sigma_{turb}^2}$ is the total 1D gas velocity dispersion, $R = FWHM_{mean}$ is the radius of the core, and G is the gravitational constant. Similarly, the thermal virial mass

M_{th} and the turbulent virial mass M_{turb} can be derived by replacing σ_{tot} with σ_{th} or σ_{turb} , respectively. The ordered magnetic virial mass is given by

$$M_B = \frac{\pi R^2 B}{\sqrt{\frac{3(3-a)}{2(5-2a)}\mu_0\pi G}}, \quad (24)$$

in SI units or CGS units. The total virial mass accounting for both the ordered magnetic field and the kinetic motions is given by

$$M_{k+B} = \sqrt{M_B^2 + \left(\frac{M_k}{2}\right)^2} + \frac{M_k}{2}. \quad (25)$$

The corresponding total virial parameter is

$$\alpha_{k+B} = \frac{M_{k+B}}{M}. \quad (26)$$

As indicated in Table 4, the turbulent magnetic energy is comparable to the ordered magnetic energy. If we take into account the turbulent magnetic energy in the virial analysis, the modified magnetic virial mass M_B^{mod} , total virial mass M_{k+B}^{mod} , and total virial parameter α_{k+B}^{mod} could be derived from Equations (24), (25), and (26) by replacing B with $B(1 + B_t^2/B_0^2)^{\frac{1}{2}}$.

Table 5 lists the calculated parameters of the two cores. The nonthermal kinetic energy, thermal kinetic energy, and ordered magnetic energy can be compared by the square of the 3D turbulent velocity dispersion ($\sigma_{turb,3D}$), 3D thermal velocity dispersion ($\sigma_{th,3D}$), and 3D Alfvén velocity ($V_{A,3D}$). Both cores have $(\sigma_{turb,3D})^2 \gg (\sigma_{th,3D})^2$ (supersonic) and $(V_{A,3D})^2 \gg (\sigma_{th,3D})^2$, which means the thermal energy only plays a negligible role in the energy balance. The two cores also have $(\sigma_{turb,3D})^2 > (V_{A,3D})^2$, suggesting that the turbulent energy exceeds the ordered magnetic energy. Another way to assess the role of the three forces is to compare the maximum mass that can be supported by each force. The mass ratios show similar trends to the energy ratios in the two cores, except that the magnetic virial mass is larger than the turbulent virial mass in MM4-Core4, which is in contrast to the energy ratio of this core ($E_{turb} > E_B$).

The modified total virial parameters α_{k+B}^{mod} in MM1-Core1 and MM4-Core4 are found to be less than 1 (i.e., subvirial). As shown in many previous studies, the main uncertainty comes from the mass estimation. If the mass is overestimated by a factor of 2 (i.e., the magnetic field strength overestimated by a factor of $\sqrt{2}$, if we ignore other sources of uncertainties), the α_{k+B}^{mod} of MM1-Core1 and MM4-Core4 would be 1.3 and 0.58, respectively. Since the α_{k+B}^{mod} in MM4-Core4 is much less than 1, it is very unlikely that MM4-Core4 is in virial equilibrium even with consideration of the large uncertainty of the analysis. However, we cannot rule out the possibility that MM1-Core1 is in virial equilibrium. More accurate estimations of the dust opacity might be required to reduce the uncertainty of the estimated virial parameter of MM1-Core1. Due to the limited angular resolution of our polarization observations and the lack of observations of appropriate turbulence tracers, we refrain from discussing the virial parameters at condensation scale.

4.2.2. Nonequilibrium Massive Star Formation

Previous observations show that a significant amount of massive star-forming clumps and cores are in subvirial states

Table 5
Physical Parameters Relevant to the Virial Analysis

Source	$\sigma_{\text{th},3\text{D}}$ (km s^{-1})	$\sigma_{\text{turb},3\text{D}}$ (km s^{-1})	$V_{\text{A},3\text{D}}$ (km s^{-1})	M (M_{\odot})	M_{th} (M_{\odot})	M_{turb} (M_{\odot})	M_{B} (M_{\odot})	$M_{\text{B}}^{\text{mod}}$ (M_{\odot})	$M_{\text{k+B}}$ (M_{\odot})	$M_{\text{k+B}}^{\text{mod}}$ (M_{\odot})	$\alpha_{\text{k+B}}$	$\alpha_{\text{k+B}}^{\text{mod}}$
MM1-Core1	0.33	2.42	1.5	212.4	1.9	102.8	61.1	95.5	132.8	161.2	0.63	0.76
MM4-Core4	0.24	0.80	0.51	42.6	0.58	6.6	7.3	11.4	11.8	15.6	0.28	0.37

(Pillai et al. 2011; Kauffmann et al. 2013; Tan et al. 2013; Liu et al. 2015; Zhang et al. 2015; Ohashi et al. 2016; Sanhueza et al. 2017; Lu et al. 2018). However, there are no direct measurements of the magnetic field strength in their analyses, while the magnetic field could provide significant support to regulate the high-mass star formation (Frau et al. 2014; Pillai et al. 2015).

Our observations and calculations offer direct evidence of the role of magnetic fields in the dynamical state of two massive dense cores. As discussed in Section 4.2.1, MM4-Core4 is in a subvirial state and MM1-Core1 is likely in a subvirial state as well. The subvirial state indicates that massive dense cores could undergo dynamical collapse in nonequilibrium in the early stage of star formation, which is in agreement with the competitive accretion model. Considering that MM1-Core1 is in a later evolutionary stage than MM4-Core4 (Zhang et al. 2009), the higher virial parameter of MM1-Core1 might suggest enhanced support from the gas motion and the magnetic field as cores evolve.

4.3. Comparing the Outflow Axis with Magnetic Field Orientation in Condensation

The importance of magnetic fields in star formation can be studied by comparing the orientations of molecular outflows and ambient magnetic fields. Results from MHD simulations (Lee et al. 2017) suggest that strong ambient magnetic fields tend to align the axis of protostellar outflows because of magnetic braking (Allen et al. 2003), while the outflow-field orientation in the weak-field case is more random.

Observationally, a compilation of all of the outflow-versus-magnetic-field angles derivable to date in low-mass protostellar cores shows that, overall, the magnetic fields in low-mass dense cores are randomly aligned with outflows (Hull & Zhang 2019). Galametz et al. (2018) found a bimodal distribution of the angles between the envelope-scale magnetic field orientation and outflow axis in low-mass class 0 objects, suggesting that the magnetic field could play an important role in regulating the direction of outflows in the early stage of low-mass star formation.

In the case of massive star formation region, an SMA survey toward high-mass clumps found no strong correlation between the outflow axis and the magnetic field orientation in evolved dense cores with a total of 21 outflow samples (Zhang et al. 2014). Because molecular outflows are believed to be driven by MHD winds originating in or near the circumstellar disk (Shu et al. 2000; Pudritz et al. 2006), the observed misalignment between the magnetic field orientation and the outflow axis indicates a less dynamically important role of magnetic fields from the core scale down to the disk scale.

With ALMA CO (2-1) and SiO (5-4) observations, Kong et al. (2019) has determined the plane-of-sky position angle of the outflows (θ_{outflow}) in IRDC G28.34 (except those in MM1). Our polarization observations have resolved the magnetic field structure down to scales of ~ 0.02 pc, which allows us to

compare the outflow axis with the magnetic field orientation at condensation scales. Because MM1 is in a later stage of star formation and the position angle of the outflows in MM1 remains undetermined due to the complexity of the CO emission, we limit the comparison in MM4 and MM9.

The magnetic field orientation in each condensation (θ_{B}) in MM4 and MM9 is measured within one ALMA synthesized beam. There are 15 outflows in MM4 and MM9, among which 12 of them are associated with polarization detections in the condensation (see Figure 15). Figure 16 shows the angular difference between the outflow axis and the magnetic field orientation in the condensations where outflows originate for the 12 outflow samples in MM4 and MM9. The angular difference between the outflow axis and the field orientation appears to be in an approximate bimodal distribution, where the outflow axis tends to be either parallel or perpendicular to the orientation of magnetic fields. In half of the objects, the magnetic field is aligned within 10° of the outflow axis, suggesting that magnetic fields could be dynamically important from the condensation scale to the disk scale in the early stage of high-mass star formation. However, the observed magnetic field and outflow position angles are projected on the plane of sky. Observations toward larger samples of magnetic fields in IRDCs are essential to help us to rule out the possibility that the observed distribution is due to the projection effect.

4.4. Fragmentation and Clustered Star Formation in MM1

The two competing massive star formation models have different predictions regarding the fragmentation of molecular clouds. The competitive accretion model proposes that the initial fragments in molecular clouds should be in thermal Jeans mass. The fragments and protostars therein near the gravitational center can thus accrete at a higher rate and form massive stars. Alternatively, the turbulent core accretion model suggests massive stars are formed via the monolithic collapse of a massive core that is supported by turbulent pressure rather than thermal pressure.

Our observations may help to distinguish between the two models. To quantify the separation of condensations in MM1, we applied the minimum spanning tree (hereafter MST) technique on these condensations using the Python package MiSTree (Naidoo 2019). The MST method connects the condensations with straight lines and minimizes the sum of the line length. Figure 17 show the MST for MM1. The separation of condensations in MM1 ranges from 0.025 to 0.16 pc.

Since the maximum recoverable scale of our ALMA observations is $\sim 7''$ for MM1, we focus on interpreting the fragmentation in the core MM1-Core1 (including Condensations 1, 2, 3, 4, 5, and 6) that has a size of $\sim 6''$. The separation of condensations in MM1-Core1 ranges from 0.025 to 0.058 pc, and the average separation ($L_{\text{av,MST}}$) of these condensations is calculated to be 0.044 pc. As the measured separations are projected on the plane-of-sky, we multiplied the observed separation by a factor of $\pi/2$ to correct for the

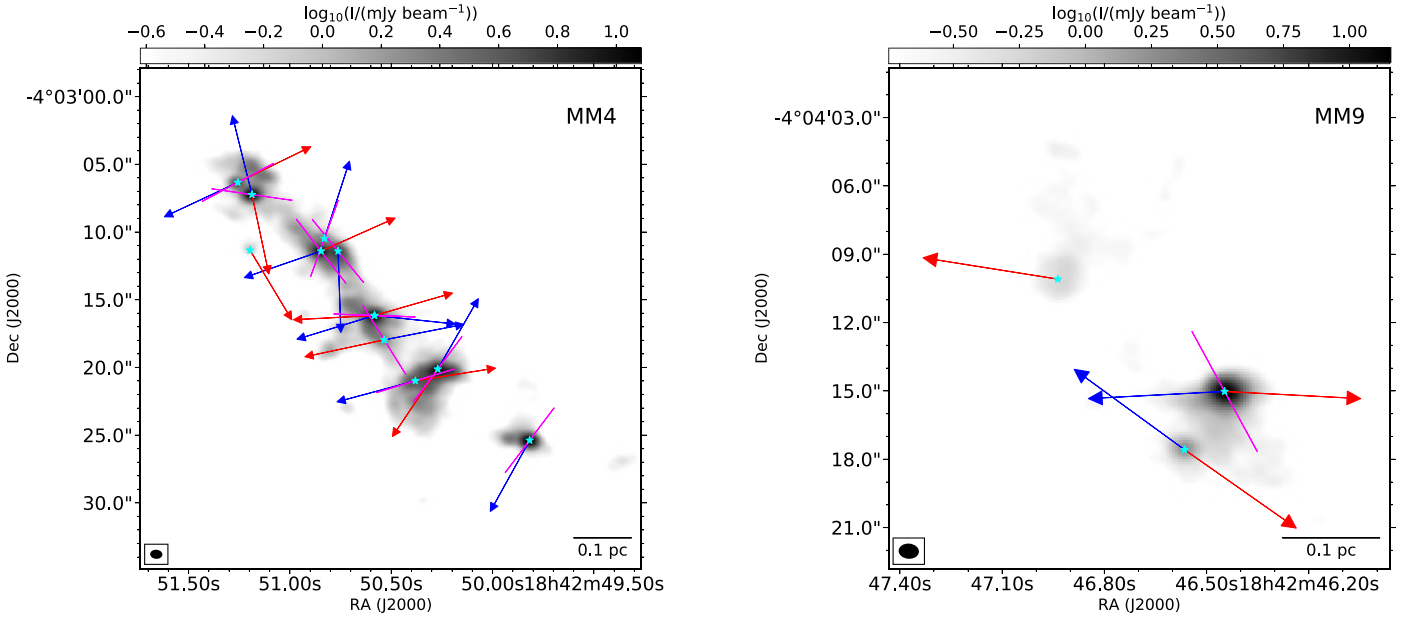


Figure 15. Summary of orientations of magnetic fields and outflows in MM4 and MM9. Stokes I of the 1.3 mm continuum is shown in gray scale. Star symbols denote the position of dense condensations (Zhang et al. 2015; Kong 2019) that are associated with outflows. Large magenta bars indicate the average magnetic orientation for each condensation. Blue- and redshifted outflow lobes are shown as blue and red dashed arrows, respectively. Bars and arrows are of arbitrary unit length.

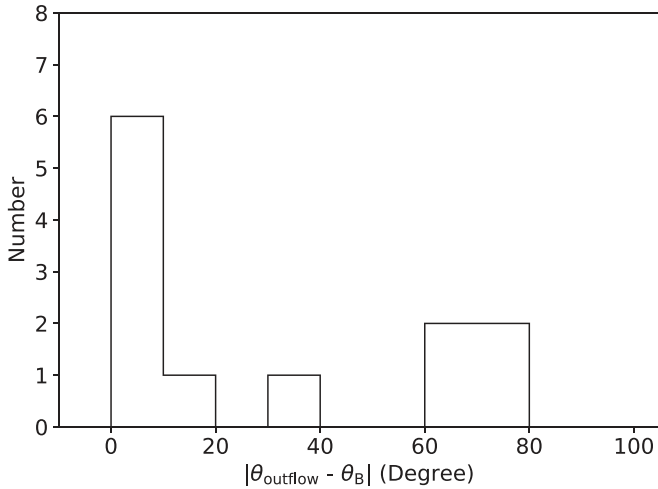


Figure 16. Angular difference between the outflow axis and the ~ 0.02 pc scale magnetic field orientation in the condensations where outflows originate for the 12 outflow samples in MM4 and MM9.

statistical projection effect (Sanhueza et al. 2019), and the corrected average separation ($L_{av,MST,cor}$) is estimated to be 0.069 pc. The mass of the condensations in MM1-Core1 ranges from 3.7 to 35.5 M_{\odot} (see Table 3) and the average mass (M_{av}) of these condensations is calculated to be 14.3 M_{\odot} .

With a temperature of 30 K and a density of $3.2 \times 10^6 \text{ cm}^{-3}$, the thermal Jeans length

$$\lambda_{J,th} = \sigma_{th,3D} \sqrt{\frac{\pi}{G\mu_{H_2} m_{HNH_2}}} \quad (27)$$

and the thermal Jeans mass

$$M_{J,th} = \frac{4}{3} \pi \mu_{H_2} m_{HNH_2} \left(\frac{\lambda_{J,th}}{2} \right)^3 \quad (28)$$

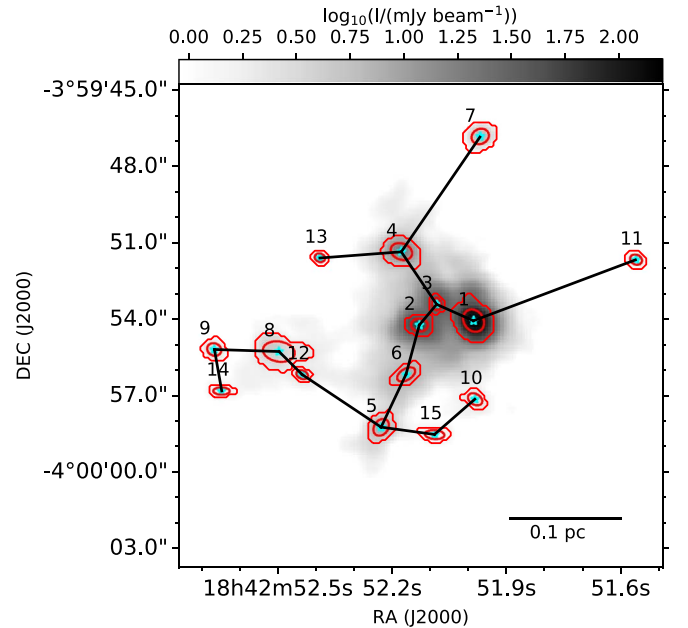


Figure 17. Results of the MST (shown in black segments) in MM1. Red contours and ellipses are the same as those in Figure 3. Star symbols mark the position of the condensations identified by dendrogram.

of MM1-Core1 are estimated to be 0.019 pc and 0.76 M_{\odot} , respectively. The M_{av} is about 19 times larger than the $M_{J,th}$ and the $L_{av,MST,cor}$ is about three times larger than the $\lambda_{J,th}$. Considering that the resolution of our observations (~ 0.02 pc) is insufficient to resolve the foreshortened thermal Jeans length ($2/\pi$ times $\lambda_{J,th}$) of 0.012 pc, we cannot rule out the possibility that the detected condensations would further fragment into smaller structures with separations $\sim \lambda_{J,th}$. However, even if each condensation in MM1-Core1 further fragments into several smaller structures, the average mass of the fragments

is unlikely to be close to the $M_{J,\text{th}}$, because M_{av} is much larger than $M_{J,\text{th}}$.

Replacing the thermal velocity dispersion with the turbulent velocity dispersion in Equations (27) and (28), the turbulent Jeans length and the turbulent Jeans mass in MM1-Core1 are estimated to be 0.14 pc and $309 M_{\odot}$, respectively, values that are much larger than the $L_{\text{av,MST,cor}}$ and the M_{av} .

Thus, we conclude that the fragmentation in MM1-Core1 cannot be explained solely by the thermal Jeans fragmentation or the turbulent Jeans fragmentation, which are inconsistent with either the competitive accretion model or the turbulent core accretion model. These discrepancies indicate that the physical condition in MM1-Core1 might have deviated from the initial condition of the core that controls the fragmentation process. On the other hand, we find that the mass of the condensations near the core center is more massive than that of the condensations in the outer region (see Table 3). Thus, we expect MM1 to form a cluster of stars with several massive stars near the center and a population of low-mass stars in the outer region. This picture seems to agree with the competitive accretion model.

5. Summary

With ALMA 1.3 mm dust polarization observations, we have presented a study of the magnetic field of three massive clumps in the IRDC G28.34. The main conclusions are as follows:

1. Polarized dust emissions are detected in all three clumps. The magnetic field morphology varies in different regions. Trends of decreasing polarization percentage with increasing intensity are detected in MM1 and MM4. The P - I relation in MM1 is shallower than that in MM4, which might be explained by the improved grain alignment efficiency due to enhanced internal radiation in more evolved regions.
2. From the dust polarization maps, we measured the plane-of-sky magnetic field strength in two massive dense cores, MM1-Core1 ($M = 212.4 M_{\odot}$) and MM4-Core4 ($M = 43.0 M_{\odot}$), with the autocorrelation function method. The B_{pos} is found to be ~ 1.6 mG and ~ 0.32 mG in MM1-Core1 and MM4-Core4, respectively.
3. We studied the dynamical state in MM1-Core1 and MM4-Core4 by calculating the virial parameter that includes both the turbulence and the magnetic field. Comparison of the energy and the virial mass indicates that turbulence dominates magnetic fields in MM1-Core1, while the magnetic field has an importance similar to that of turbulence in MM4-Core4. The results of the virial analysis suggest that MM4-Core4 is in a subvirial state and MM1-Core1 is likely in a subvirial state as well, which signifies a dynamical massive star formation in nonequilibrium.
4. We compared the orientations of the magnetic field, local gravity, and intensity gradient, with the polarization-intensity gradient-local gravity method. We found that the intensity gradient closely follows the local gravity in the three clumps. The magnetic field is found to be randomly aligned with the intensity gradient, but better aligned with the local gravity in MM1 and MM4. The average ratio of magnetic field to gravity force is found to be smaller than 1 in both MM1 and MM4, which

suggests that the magnetic force alone cannot prevent the gravitational collapse.

5. With a total of 12 outflow samples in MM4 and MM9, the angle between orientations of the magnetic field at condensation scales and the outflow axis shows an approximately bimodal distribution with half of the outflows aligned within 10° of the magnetic field, which suggests that magnetic fields could play an important role from the condensation scale to the disk scale in the early stage of massive star formation.
6. We identified the dense condensations in MM1 with the dendrogram method, and characterized the separation of these condensations using the minimum spanning tree technique. The mass of the condensations and the average minimum separation between condensations in MM1-Core1 are found to be larger than the values predicted by thermal Jeans fragmentation and smaller than the values predicted by turbulent Jeans fragmentation. Thus, we propose that the physical condition in MM1-Core1 might have deviated from the initial condition that controls the fragmentation.

We thank Dr. Diego Falceta-Gonçalves, Dr. J. Michail, and Dr. Fabio Santos for sharing their codes for plotting the LIC maps, and Dr. Shuo Kong for sharing the catalog of the outflows in G28.34. We are indebted to the anonymous referee, whose constructive comments improved the presentation and clarity of the paper. K.Q. and J.L. are supported by National Key R&D Program of China No. 2017YFA0402600. K.Q. and J.L. acknowledge support from the National Natural Science Foundation of China (NSFC) through grants U1731237, 11590781, and 11629302. J.L. acknowledges support from the program of the China Scholarship Council (No. 201806190134) and from the Smithsonian Astrophysical Observatory predoctoral fellowship. J.M.G. is supported by the Spanish grant AYA2017-84390-C2-R (AEI/FEDER, UE). Z.Y.L. is supported in part by NASA 80NSSC18K1095 and NSF AST-1716259 and 1815784. This paper makes use of the following ALMA data: ADS/JAO.ALMA#2016.1.00248.S and ADS/JAO.ALMA#2017.1.00793.S. ALMA is a partnership of the ESO (representing its member states), NSF (USA) and NINS (Japan), together with NRC (Canada), MOST and ASIAA (Taiwan), and KASI (Republic of Korea), in cooperation with the Republic of Chile. The Joint ALMA Observatory is operated by ESO, AUI/NRAO, and NAOJ. The National Radio Astronomy Observatory is a facility of the National Science Foundation operated under cooperative agreement by Associated Universities, Inc. This research made use of the following software: *astrodendro*, a Python package to compute dendrograms of Astronomical data (<http://www.dendrograms.org/>); *APLpy*, an open-source plotting package for Python (Robitaille & Bressert 2012); *Astropy*, a community-developed core Python package for Astronomy (Astropy Collaboration et al. 2013); and *Matplotlib*, a Python 2D plotting library for Python (Hunter 2007).

Facility: Atacama Large Millimeter/Submillimeter Array (ALMA).

Software: *APLpy* (Robitaille & Bressert 2012), *Astropy* (Astropy Collaboration et al. 2013), *Matplotlib* (Hunter 2007).

Appendix Virial Theorem

Ignoring the surface kinetic energy, the virial theorem is written as:

$$\frac{1}{2} \frac{d^2 I}{dt^2} = 2E_k + E_B + E_G, \quad (\text{A1})$$

where I is the moment of inertia, E_k is the kinetic energy, E_B is the magnetic energy, and E_G is the gravitational energy. For a sphere with a radial density profile $\rho \propto r^{-a}$ (for a uniform density, $a = 0$), the gravitational energy is given by

$$E_G = -\frac{(3-a)}{(5-2a)} \frac{GM^2}{R}, \quad (\text{A2})$$

where G is the gravitational constant, M is the mass of the considered structure, and R is the radius of the structure. The magnetic energy is given by

$$E_B = \frac{B^2 V}{2\mu_0}, \quad (\text{A3})$$

where $V = 4\pi R^3/3$ is the volume of the structure. The kinetic energy is the sum of the thermal energy (E_{th}) and the turbulent energy (E_{turb}):

$$E_k = E_{\text{th}} + E_{\text{turb}} = \frac{3}{2} M \sigma_{\text{tot}}^2, \quad (\text{A4})$$

where σ_{tot} is the total 1D gas velocity dispersion. The thermal energy and the turbulent energy can be derived by

$$E_{\text{th}} = \frac{3}{2} M \sigma_{\text{th}}^2, \quad (\text{A5})$$

and

$$E_{\text{turb}} = \frac{3}{2} M \sigma_{\text{turb}}^2, \quad (\text{A6})$$

respectively, where σ_{th} is the 1D thermal velocity dispersion and σ_{turb} is the 1D turbulent velocity dispersion.

For a nonmagnetized ($E_B = 0$) sphere, the structure is stable when $2E_k + E_G < 0$, which requires $M < M_k$, where

$$M_k = \frac{3(5-2a)\sigma_{\text{tot}}^2 R}{(3-a)G} \quad (\text{A7})$$

is the kinetic virial mass. Similarly, we can define the thermal virial mass M_{th} and the turbulent virial mass M_{turb} by replacing σ_{tot} with the corresponding velocity dispersion to account for the thermal component and the turbulent component of the virial mass separately. Bertoldi & McKee (1992) introduced a kinetic virial parameter

$$\alpha_k = \frac{2E_k}{|E_G|} = \frac{3(5-2a)\sigma_{\text{tot}}^2 R}{(3-a)GM} = \frac{M_k}{M} \quad (\text{A8})$$

to represent the ratio of the kinetic energy and the gravitational energy. We note that $M < M_k$ (kinetically supervirial) is equivalent to $\alpha_k > 1$. For comparison with M_k , a Bonnor–Ebert sphere (Bonnor 1956; Ebert 1957) in isothermal hydrostatic equilibrium is stable when $M < M_{\text{BE}}$, where M_{BE} is the

Bonnor–Ebert critical mass given by

$$M_{\text{BE}} = 2.43 \frac{\sigma_{\text{tot}}^2 R}{G}. \quad (\text{A9})$$

For a uniform sphere ($a = 0$), $M < M_{\text{BE}}$ is equivalent to $\alpha_k > 2.06$.

If the kinetic energy is negligible ($E_k = 0$), a stable sphere has $E_B + E_G < 0$, which implies $M < M_B$, where

$$M_B = \frac{\pi R^2 B}{\sqrt{\frac{3(3-a)}{2(5-2a)} \mu_0 \pi G}} \quad (\text{A10})$$

is the magnetic virial mass in SI units or CGS units. We noticed that some previous studies (e.g., Hennebelle & Chabrier 2008; Pillai et al. 2011; Ohashi et al. 2016; Sanhueza et al. 2017; Hull & Zhang 2019) have written the magnetic virial mass of a uniform ($a = 0$) sphere as

$$M'_B = \frac{5RV_{\text{A,3D}}^2}{6G} = \frac{5RB^2}{6\mu_0 \rho G} = \frac{10\pi R^4 B^2}{9\mu_0 GM}, \quad (\text{A11})$$

where $V_{\text{A,3D}} = \frac{B}{\sqrt{\mu_0 \rho}}$ is the 3D Alfvén velocity in SI units or CGS units. The M'_B is derived by writing the magnetic energy as

$$E'_B = \frac{B^2 M}{2\mu_0 \rho} \quad (\text{A12})$$

and solving the critical mass for $E'_B + E_G = \frac{B^2 M}{2\mu_0 \rho} - \frac{3GM^2}{5R} < 0$. However, we point out that, since M , ρ , and R are not independent ($M = 4\pi R^3 \rho/3$), the magnetic virial mass should be written as a function of either R or ρ , but not both R and ρ . Thus, M'_B does not accurately estimate the magnetic virial mass. For a magnetically supercritical ($M > M_B$) structure, $M'_B = \frac{10\pi R^4 B^2}{9\mu_0 GM} < \frac{10\pi R^4 B^2}{9\mu_0 GM_B} = M_B$ would underestimate the magnetic virial mass, and vice versa. For comparison with M_B , the magnetic critical mass of an isothermal disk (Nakano & Nakamura 1978) has been derived to be

$$M_{\text{B,disk}} = \frac{\pi R^2 B}{\sqrt{\mu_0 \pi G}}. \quad (\text{A13})$$

Crutcher et al. (2004) introduced a parameter λ to state the mass-to-flux ratio in units of its critical value:

$$\lambda = \frac{(M/\Phi)_{\text{observed}}}{(M/\Phi)_{\text{critical}}} = \frac{M}{M_{\text{B,disk}}}, \quad (\text{A14})$$

where $(M/\Phi)_{\text{observed}}$ is the observed ratio of mass to magnetic flux:

$$\left(\frac{M}{\Phi}\right)_{\text{observed}} = \frac{\mu_{\text{H}_2} m_{\text{H}} N(\text{H}_2)}{B}, \quad (\text{A15})$$

and $(M/\Phi)_{\text{critical}}$ is the critical ratio of mass to magnetic flux:

$$\left(\frac{M}{\Phi}\right)_{\text{critical}} = \frac{1}{\sqrt{\mu_0 \pi G}}. \quad (\text{A16})$$

For a magnetically subcritical structure with mass less than the magnetic critical mass, the magnetic field alone can prevent the structure from collapse.

Taking into account both the magnetic energy and the kinetic energy, a structure is stable when $2E_k + E_B + E_G < 0$. The critical virial mass is calculated to be

$$M_{k+B} = \sqrt{M_B^2 + \left(\frac{M_k}{2}\right)^2} + \frac{M_k}{2}. \quad (\text{A17})$$

It should be noted that $M_k + M_B$ is systematically larger than M_{k+B} (Bertoldi & McKee 1992), and the largest ratio between $M_k + M_B$ and M_{k+B} is 1.25 when $M_B = 0.67M_k$. Therefore, some previous studies using $M_B + M_k$ to represent the total virial mass may have slightly overestimated the support from the magnetic field and gas motion. Following the definition of α_k , we can define a total virial parameter


$$\alpha_{k+B} = \frac{M_{k+B}}{M}. \quad (\text{A18})$$


ORCID iDs

Junhao Liu  <https://orcid.org/0000-0002-4774-2998>

Qizhou Zhang  <https://orcid.org/0000-0003-2384-6589>

Keping Qiu  <https://orcid.org/0000-0002-5093-5088>

Hauyu Baobab Liu  <https://orcid.org/0000-0003-2300-2626>

Thushara Pillai  <https://orcid.org/0000-0003-2133-4862>

Josep Miquel Girart  <https://orcid.org/0000-0002-3829-5591>

References

- Allen, A., Li, Z.-Y., & Shu, F. H. 2003, *ApJ*, 599, 363
- Andersson, B.-G., Lazarian, A., & Vaillancourt, J. E. 2015, *ARA&A*, 53, 501
- Astropy Collaboration, Robitaille, T. P., Tollerud, E. J., et al. 2013, *A&A*, 558, A33
- Beckwith, S. V. W., & Sargent, A. I. 1991, *ApJ*, 381, 250
- Bertoldi, F., & McKee, C. F. 1992, *ApJ*, 395, 140
- Beuther, H., Leurini, S., Schilke, P., et al. 2007, *A&A*, 466, 1065
- Beuther, H., Soler, J. D., Vlemmings, W., et al. 2018, *A&A*, 614, A64
- Bonnell, I. A., Bate, M. R., Clarke, C. J., et al. 1997, *MNRAS*, 285, 201
- Bonnor, W. B. 1956, *MNRAS*, 116, 351
- Butler, M. J., & Tan, J. C. 2009, *ApJ*, 696, 484
- Cabral, B., & Leedom, L. C. 1993, in Proc. 20th Annual Conf. on Computer Graphics and Interactive Techniques, ed. M. C. Whittom (New York: ACM), 263, <https://dl.acm.org/citation.cfm?id=166151>
- Cao, Y., Qiu, K., Zhang, Q., et al. 2019, *ApJS*, 241, 1
- Carey, S. J., Clark, F. O., Egan, M. P., et al. 1998, *ApJ*, 508, 721
- Chandrasekhar, S., & Fermi, E. 1953, *ApJ*, 118, 113
- Chen, H.-R., Liu, S.-Y., Su, Y.-N., et al. 2010, *ApJL*, 713, L50
- Chen, H.-R., Su, Y.-N., Liu, S.-Y., et al. 2007, *ApJL*, 654, L87
- Cheng, Y., Tan, J. C., Liu, M., et al. 2018, *ApJ*, 853, 160
- Crutcher, R. M., Nutter, D. J., Ward-Thompson, D., et al. 2004, *ApJ*, 600, 279
- Davis, L. 1951, *PhRv*, 81, 890
- Ebert, R. 1957, *ZA*, 42, 263
- Falceta-Gonçalves, D., Lazarian, A., & Kowal, G. 2008, *ApJ*, 679, 537
- Feng, S., Beuther, H., Zhang, Q., et al. 2016a, *ApJ*, 828, 100
- Feng, S., Beuther, H., Zhang, Q., et al. 2016b, *A&A*, 592, A21
- Feng, S., Caselli, P., Wang, K., et al. 2019, *ApJ*, 883, 202
- Frau, P., Girart, J. M., Zhang, Q., et al. 2014, *A&A*, 567, A116
- Galametz, M., Maury, A., Girart, J. M., et al. 2018, *A&A*, 616, A139
- Girart, J. M., Beltrán, M. T., Zhang, Q., et al. 2009, *Sci*, 324, 1408
- Girart, J. M., Frau, P., Zhang, Q., et al. 2013, *ApJ*, 772, 69
- Heitsch, F., Zweibel, E. G., mac Low, M.-M., et al. 2001, *ApJ*, 561, 800
- Hennebelle, P., & Chabrier, G. 2008, *ApJ*, 684, 395
- Henning, T., Michel, B., & Stognienko, R. 1995, *P&SS*, 43, 1333
- Hildebrand, R. H. 1983, *QJRAS*, 24, 267
- Hildebrand, R. H., Kirby, L., Dotson, J. L., Houde, M., & Vaillancourt, J. E. 2009, *ApJ*, 696, 567
- Ho, P. T. P., & Townes, C. H. 1983, *ARA&A*, 21, 239
- Houde, M., Hull, C. L. H., Plambeck, R. L., et al. 2016, *ApJ*, 820, 38
- Houde, M., Vaillancourt, J. E., Hildebrand, R. H., Chitsazzadeh, S., & Kirby, L. 2009, *ApJ*, 706, 1504
- Hull, C. L. H., & Zhang, Q. 2019, *FrASS*, 6, 3
- Hunter, J. D. 2007, *CSE*, 9, 90
- Juvela, M., Guillet, V., Liu, T., et al. 2018, *A&A*, 620, A26
- Kataoka, A., Muto, T., Momose, M., et al. 2015, *ApJ*, 809, 78
- Kauffmann, J., Pillai, T., & Goldsmith, P. F. 2013, *ApJ*, 779, 185
- Kirk, J. M., Ward-Thompson, D., Palmeirim, P., et al. 2013, *MNRAS*, 432, 1424
- Koch, P. M., Tang, Y.-W., & Ho, P. T. P. 2012, *ApJ*, 747, 79
- Kong, S. 2019, *ApJ*, 873, 31
- Kong, S., Arce, H. G., Maureira, M. J., et al. 2019, *ApJ*, 874, 104
- Kong, S., Tan, J. C., Arce, H. G., et al. 2018a, *ApJL*, 855, L25
- Kong, S., Tan, J. C., Caselli, P., et al. 2018b, *ApJ*, 867, 94
- Krumholz, M. R. 2014, *PhR*, 539, 49
- Krumholz, M. R., McKee, C. F., & Klein, R. I. 2005, *Natur*, 438, 332
- Kwon, J., Doi, Y., Tamura, M., et al. 2018, *ApJ*, 859, 4
- Lazarian, A. 2007, *JQSRT*, 106, 225
- Lazarian, A., & Hoang, T. 2007, *MNRAS*, 378, 910
- Lee, J. W. Y., Hull, C. L. H., & Offner, S. S. R. 2017, *ApJ*, 834, 201
- Lin, Y., Liu, H. B., Dale, J. E., et al. 2017, *ApJ*, 840, 22
- Liu, H. B., Galván-Madrid, R., Jiménez-Serra, I., et al. 2015, *ApJ*, 804, 37
- Liu, J., Qiu, K., Berry, D., et al. 2019, *ApJ*, 877, 43
- Liu, M., Tan, J. C., Cheng, Y., et al. 2018a, *ApJ*, 862, 105
- Liu, T., Li, P. S., Juvela, M., et al. 2018b, *ApJ*, 859, 151
- Lu, X., Zhang, Q., Liu, H. B., et al. 2018, *ApJ*, 855, 9
- McKee, C. F., & Tan, J. C. 2002, *Natur*, 416, 59
- McMullin, J. P., Waters, B., Schiebel, D., et al. 2007, in ASP Conf. Ser. 376, *Astronomical Data Analysis Software and Systems*, ed. R. A. Shaw, F. Hill, & D. J. Bell (San Francisco, CA: ASP), 127
- Motte, F., & André, P. 2001, *A&A*, 365, 440
- Motte, F., Bontemps, S., Schilke, P., et al. 2007, *A&A*, 476, 1243
- Naghizadeh-Khouei, J., & Clarke, D. 1993, *A&A*, 274, 968
- Naidoo, K. 2019, *JOSS*, 4, 1721
- Nakano, T., & Nakamura, T. 1978, *PASJ*, 30, 671
- Ohashi, S., Sanhueza, P., Chen, H.-R. V., et al. 2016, *ApJ*, 833, 209
- Ostriker, E. C., Stone, J. M., & Gammie, C. F. 2001, *ApJ*, 546, 980
- Padoan, P., Goodman, A., Draine, B. T., et al. 2001, *ApJ*, 559, 1005
- Pattle, K., & Fissel, L. 2019, *FrASS*, 6, 15
- Pattle, K., Lai, S.-P., Hasegawa, T., et al. 2019, *ApJ*, 880, 27
- Pattle, K., Ward-Thompson, D., Berry, D., et al. 2017, *ApJ*, 846, 122
- Pattle, K., Ward-Thompson, D., Kirk, J. M., et al. 2015, *MNRAS*, 450, 1094
- Perauld, M., Omont, A., Simon, G., et al. 1996, *A&A*, 315, L165
- Pillai, T., Kauffmann, J., Tan, J. C., et al. 2015, *ApJ*, 799, 74
- Pillai, T., Kauffmann, J., Wyrowski, F., et al. 2011, *A&A*, 530, A118
- Pillai, T., Wyrowski, F., Carey, S. J., et al. 2006, *A&A*, 450, 569
- Pudritz, R. E., Rogers, C. S., & Ouyed, R. 2006, *MNRAS*, 365, 1131
- Qiu, K., Zhang, Q., Menten, K. M., et al. 2014, *ApJL*, 794, L18
- Ragan, S., Henning, T., Krause, O., et al. 2012, *A&A*, 547, A49
- Rao, R., Crutcher, R. M., Plambeck, R. L., et al. 1998, *ApJL*, 502, L75
- Rathborne, J. M., Jackson, J. M., & Simon, R. 2006, *ApJ*, 641, 389
- Robitaille, T., & Bressert, E. 2012, *APLpy: Astronomical Plotting Library in Python*, *Astrophysics Source Code Library*, ascl:1208.017
- Rosolowsky, E. W., Pineda, J. E., Kauffmann, J., et al. 2008, *ApJ*, 679, 1338
- Roy, A., André, P., Palmeirim, P., et al. 2014, *A&A*, 562, A138
- Sanhueza, P., Contreras, Y., Wu, B., et al. 2019, *ApJ*, 886, 102
- Sanhueza, P., Jackson, J. M., Zhang, Q., et al. 2017, *ApJ*, 841, 97
- Shu, F. H., Adams, F. C., & Lizano, S. 1987, *ARA&A*, 25, 23
- Shu, F. H., Najita, J. R., Shang, H., & Li, Z.-Y. 2000, in *Protostars and Planets IV*, ed. V. Manning, A. P. Boss, & S. S. Russell (Tucson, AZ: Univ. Arizona Press), 789
- Simon, R., Rathborne, J. M., Shah, R. Y., et al. 2006, *ApJ*, 653, 1325
- Soam, A., Liu, T., Andersson, B.-G., et al. 2019, *ApJ*, 883, 95
- Soam, A., Pattle, K., Ward-Thompson, D., et al. 2018, *ApJ*, 861, 65
- Tan, J. C., Beltrán, M. T., Caselli, P., et al. 2014, in *Protostars and Planets VI*, ed. H. Beuther et al. (Tucson, AZ: Univ. Arizona Press), 149
- Tan, J. C., Kong, S., Butler, M. J., et al. 2013, *ApJ*, 779, 96
- Tan, J. C., Kong, S., Zhang, Y., et al. 2016, *ApJL*, 821, L3
- Tang, Y.-W., Ho, P. T. P., Girart, J. M., et al. 2009, *ApJ*, 695, 1399
- Tang, Y.-W., Koch, P. M., Peretto, N., et al. 2019, *ApJ*, 878, 10
- Tazaki, R., Lazarian, A., & Nomura, H. 2017, *ApJ*, 839, 56

Terebey, S., Chandler, C. J., & Andre, P. 1993, [ApJ](#), 414, 759
Vaillancourt, J. E. 2006, [PASP](#), 118, 1340
Wang, K., Zhang, Q., Wu, Y., et al. 2011, [ApJ](#), 735, 64
Wang, K., Zhang, Q., Wu, Y., et al. 2012, [ApJL](#), 745, L30
Wang, Ke. 2018, [RNAAS](#), 2, 52
Wang, Y., Zhang, Q., Pillai, T., et al. 2008, [ApJL](#), 672, L33

Wang, Y., Zhang, Q., Rathborne, J. M., et al. 2006, [ApJL](#), 651, L125
Ward-Thompson, D., Pattle, K., Bastien, P., et al. 2017, [ApJ](#), 842, 66
Yang, H., Li, Z.-Y., Looney, L., et al. 2016, [MNRAS](#), 456, 2794
Zhang, Q., Qiu, K., Girart, J. M., et al. 2014, [ApJ](#), 792, 116
Zhang, Q., Wang, K., Lu, X., et al. 2015, [ApJ](#), 804, 141
Zhang, Q., Wang, Y., Pillai, T., et al. 2009, [ApJ](#), 696, 268